

Critical Filaments and Superconductivity in Quasiperiodic Twisted Bilayer Graphene

Xinghai Zhang,¹ Justin H. Wilson,^{2,3} and Matthew S. Foster^{1,4}

¹*Department of Physics and Astronomy, Rice University, Houston, Texas 77005, USA*

²*Department of Physics and Astronomy, Louisiana State University, Baton Rouge, LA 70803, USA*

³*Center for Computation and Technology, Louisiana State University, Baton Rouge, LA 70803, USA*

⁴*Rice Center for Quantum Materials, Rice University, Houston, Texas 77005, USA*

(Dated: January 20, 2025)

Multilayer moiré materials can exhibit topological electronic features yet are inherently quasiperiodic—leading to wave function interference whose Anderson-localizing tendency can be mitigated by topology. We consider a quasiperiodic variant of the chiral Bistritzer-MacDonald model for twisted bilayer graphene with two incommensurate moiré potentials that serves as a toy model for twisted trilayer. We observe “filaments” linking magic angles with enhanced density of states and fractal wave functions that evade localization; states away from the filaments mimic fractal surface states of dirty topological superconductors. We demonstrate that topological quasiperiodicity can broadly enhance superconductivity *without* magic-angle fine-tuning.

I. INTRODUCTION

Amplifying electronic interactions and uncovering topological phases drives much of the research in moiré materials [1]. Correlated phases including superconductivity were observed in twisted bilayer graphene (TBLG) [1], attributed to enhanced interactions due to flattening of the moiré bands near magic angles [2–5]. Concurrently, topology is enabled in TBLG by the coupling of same-chirality Dirac electrons between the layers [6–9].

Generic twist angles in moiré materials lead to incommensurate (quasiperiodic) tunneling, but this has negligible effects in TBLG. By contrast, quasiperiodicity is ubiquitous when *multiple* moiré patterns compete, as occurs in systems such as twisted trilayer graphene (TTLG), where superconductivity was recently observed [10, 11]. Previous work on quasiperiodic Dirac and moiré materials focused on tight-binding models with lattice incommensuration [12–14], and provided glimpses of a kind of wave-function criticality linked with “magic angles.” Wave-function criticality (multifractality) is typically associated to *disorder-driven* Anderson localization transitions [15]. Quasiperiodicity induces interference that can also drive Anderson localization, although the most-studied cases in one dimension (1D) show features different from random 1D systems [16, 17]. At the same time the tendency towards localization can be mitigated by topology, which protects boundary and bulk states in nontrivial bands.

The *interplay* between multifractality and interactions can produce surprising effects. For example, the average Cooper pairing amplitude can be *enhanced* near a superconductor-insulator transition if Coulomb interactions are externally screened. The mechanism involves the Russian-doll-like nesting (“Chalker scaling”) of multifractal states, and can occur near the localization transition [18, 19] and in 1D quasiperiodic models [20–22].

This raises a question: Can quasiperiodic and topological effects in multilayer moiré materials lead to criticality that enhances correlated behavior, such as superconductivity? We address this by studying a quasiperiodic vari-

ant of the chiral Bistritzer-MacDonald (BM) model for TBLG. Our model incorporates two incommensurate BM potentials as occurs in TTLG, and serves as a toy version of the latter with two layers instead of three. As we show in this paper, quasiperiodicity with topology can lead to criticality and amplify pairing *without* the need to fine-tune to magic angles, see Fig. 1.

The BM model for TBLG [2, 4] possesses an emergent particle-hole symmetry [6], falling into class C in the 10-fold classification of topological matter [26] and 2D Dirac Hamiltonians [27]. If AA tunneling vanishes, a chiral symmetry emerges [5]. This chiral BM model takes the same form as the *2D surface theory* of a bulk class CI topological superconductor (TSC) [28], while the BM model corresponds to the same surface, subject to orbital time-reversal symmetry breaking.

Quenched disorder, which respects the chiral symmetry, leads to remarkable results for class-CI TSC surface states, including a power-law vanishing density of states (DOS) $\nu(E) \sim |E|^{1/7}$ [29] and critical low-energy wave functions with universal multifractal statistics [30]. Recent results have demonstrated that a more radical kind of universal wave-function criticality can extend over a wide range of the energy spectrum for these surfaces (“spectrum-wide quantum criticality,” SWQC [23–25]).

In this paper, we show that topological quasiperiodicity leads to DOS enhancements and wave-function fractality. We establish that quasiperiodic multilayer graphene effectively simulates *disordered* TSC surface states. The resulting SWQC and absence of Anderson localization are exotic TSC features [23, 24] that are synthetically realizable in multilayer moiré materials. Our results are surprising because they precisely link the criticality of dirty surface states of bulk topological phases to quasiperiodic layered 2D materials. Since the bulk is “missing,” one might say that quasiperiodic twisted multilayers *holographically* realize bulk topological superconductor classes.

We study the consequences of topologically-protected quasiperiodicity for superconductivity using self-consistent BCS calculations [22], finding enhanced

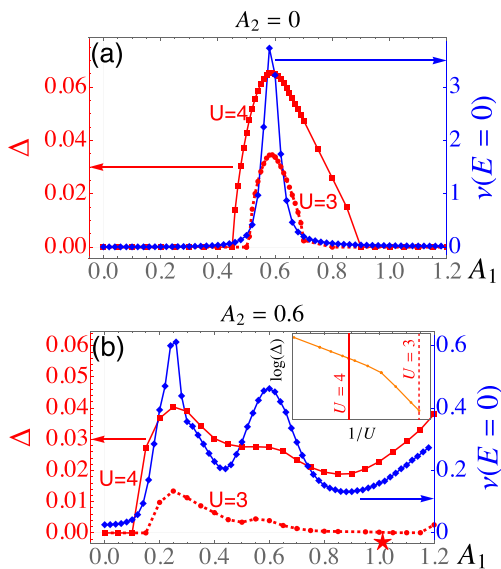


FIG. 1. (a): Pairing amplitude Δ and density of states (DOS) $\nu(E)$ for the chiral Bistritzer-MacDonald (BM) model; the enhancement of superconductivity occurs near the magic-angle ($A_1 \approx 0.586$). (b): The same for the quasiperiodic BM model; superconductivity is broadly enhanced by wave-function multifractality *without* magic-angle fine-tuning. The parameters $A_{1,2}$ are the strengths of the two incommensurate BM potentials, see Eqs. (2.1) and (2.2). All results are obtained from self-consistent BCS numerics using the kernel polynomial method (Sec. III); U is the interaction strength measured relative to the kinetic energy. The inset shows the U -dependence of Δ at $A_1 = 1$ and $A_2 = 0.6$. Here the combination of Chalker scaling and topology [23–25] leads to *BCS-like* dependence $\Delta \sim e^{-c/U}$ (see Secs. II C and VI B), instead of the threshold behavior of a 2D Dirac semimetal. The latter occurs away from the magic angle in (a).

Cooper pairing [18, 19] without fine-tuning to magic angles (Fig. 1). For simplicity, we consider intravalley pairing. Our calculations incorporate additional aspects beyond those of the normal state such as Altshuler-Aronov corrections, which can also cause Anderson localization; such corrections shift the Bogoliubov-de Gennes eigenstate localization transition in a 1D quasiperiodic model [22]. We demonstrate that this effect is absent here due to topological protection [31], and we find that the superfluid stiffness precisely encodes the topological character of the normal state (another instance of the “holography”). Our approach can be applied to the more complicated case of TTLG [32].

A. Outline

This paper is organized as follows. The main results are presented and discussed in Sec. II; we first introduce our quasiperiodic version of the chiral Bistritzer-MacDonald model and detail the setup for the numerical kernel-polynomial method (KPM) calculations. We then

summarize results for the density of states and wave-function multifractality, linking the latter to TSC surface states. Finally, we consider superconductivity and discuss further directions. The rest of the paper contains technical details. Sec. III provides a pedagogical introduction to the KPM method, particularly the implementations needed for wave function calculations, self-consistent BCS theory, and superfluid stiffness computation. Sec. IV gives additional results and details for the density of states and wave-function criticality. Sec. V summarizes results for a silver-ratio variant quasiperiodic model. Finally, Sec. VI collects additional details and results for superconductivity in the quasiperiodic chiral Bistritzer-MacDonald model.

II. MAIN RESULTS

A. Model

We consider a quasiperiodic version of the chiral Bistritzer-MacDonald (qBM) model [4, 5],

$$h(\mathbf{r}) = -iv_F \boldsymbol{\sigma} \cdot \nabla + V_{\mathbf{q}}(\mathbf{r}) + V_{\mathbf{q}'}(\mathbf{r}). \quad (2.1)$$

The Pauli matrices $\sigma_{1,2}$ act on the sublattice space, and $V_{\mathbf{q}}(\mathbf{r})$ and $V_{\mathbf{q}'}(\mathbf{r})$ denote moiré potentials coupling the two layers in AB- and BA-stacking regimes,

$$V_{\mathbf{q}}(\mathbf{r}) = A_1 [U_0(\mathbf{r}) \tau^+ \sigma^+ + U_1(\mathbf{r}) \tau^+ \sigma^- + \text{H.c.}]. \quad (2.2)$$

Here $\tau^\pm = (\tau_x \pm i\tau_y)/2$ (and similarly for σ^\pm) with τ_j as the Pauli matrices that link the layers. The potentials U_0 and U_1 take the forms [4] $U_0(\mathbf{r}) = e^{-i\mathbf{q}_1 \cdot \mathbf{r}} + e^{-i\mathbf{q}_2 \cdot \mathbf{r}} + e^{-i\mathbf{q}_3 \cdot \mathbf{r}}$ and $U_1(\mathbf{r}) = e^{-i\mathbf{q}_1 \cdot \mathbf{r}} + e^{-i\frac{2\pi}{3}\mathbf{q}_2 \cdot \mathbf{r}} + e^{i\frac{2\pi}{3}\mathbf{q}_3 \cdot \mathbf{r}}$. Here $\mathbf{q}_1 = k_\theta(1, 0)$ and $\mathbf{q}_{2/3} = k_\theta(-1/2, \pm\sqrt{3}/2)$ are the reciprocal lattice vectors of the usual moiré potential. The momentum $k_\theta = 2K \sin \theta/2$ defines the moiré scale (with K the K-point wavevector modulus in graphene). The second moiré potential $V_{\mathbf{q}'}(\mathbf{r})$ takes the same form but with different reciprocal vectors $\{\mathbf{q}'_i\}$ and potential strength A_2 . When the two sets $\{\mathbf{q}_i\}$ and $\{\mathbf{q}'_i\}$ are mutually incommensurate, we have a quasiperiodic model. In this paper, we focus on the case $\mathbf{q}_i = \beta \mathbf{q}'_i$ with β the inverse golden ratio $(\sqrt{5} - 1)/2$; we have verified that similar results obtain for other (e.g., silver) ratios, see Sec. V.

The qBM model is realized in momentum space using a momentum cutoff $\Lambda = N_\Lambda k_\theta/2$. Focusing on $V_{\mathbf{q}}(\mathbf{r})$, the moiré Brillouin zone (mBZ) has linear size k_θ , and we keep $2N_\Lambda^2$ moiré bands. Without a second potential, a momentum space lattice of linear size N_Λ is sufficient; however, \mathbf{q}'_i allows hoppings *within* the mBZ. Since $|\mathbf{q}'_i| = k_\theta/\beta$, we controllably reach larger system sizes with rational approximations of β , i.e. $\beta_n = F_n/F_{n+1}$ for Fibonacci numbers F_n . In this case, the denominator $\frac{|\mathbf{q}'_i|}{k_\theta} = \frac{F_{n+1}}{F_n}$ determines the linear size of momentum space points required within one mBZ. Therefore, the full momentum space lattice has linear size $N_\Lambda F_n$ and spacing $\Delta k = k_\theta/F_n$; in the

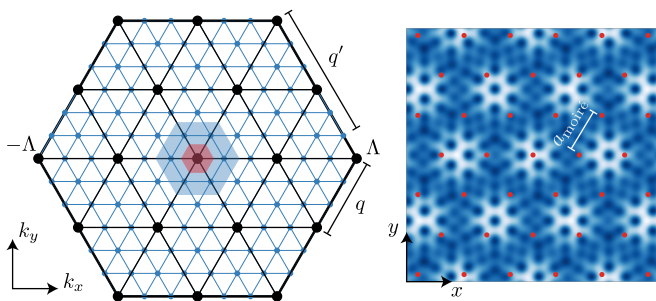


FIG. 2. (left) An illustration of the k -space grid used for $q'/q = 5/3$ and $N_\Lambda = 4$. The blue region is the moiré Brillouin zone produced by A_1 and the red region is the super-moiré Brillouin zone of the combined potentials for this commensurate fraction. (right) A density plot of $\|V_{\mathbf{q}}(\mathbf{r}) + V_{\mathbf{q}'}(\mathbf{r})\|^2$ with $A_1 = A_2$ to illustrate the quasiperiodicity. The red dots are the original moiré sites for the A_1 potential, separated by the scale $a_{\text{moiré}} = 4\pi/\sqrt{3}k_\theta$.

incommensurate limit ($n \rightarrow \infty$), all momentum can be accessed. In the following, we work in units such that $v_F = 1$ and $k_\theta = |\mathbf{q}_z| = 1$; all energies are measured in units of $v_F k_\theta$. Our setup is illustrated in Fig. 2.

B. Density of states and fractal wave functions

Dirac cones have a vanishing DOS $\nu(E) \sim |E|/v^2$ with velocity v ; at the magic angle $v \rightarrow 0$ and $\nu(0)$ diverges. In the quasiperiodic case, at small $A_{1,2}$ the semimetal is stable and eigenstates remain plane-wave-like [33]. However, when $\nu(0) > 0$ (or vanishes with a small power-law), multifractality—typically associated to an Anderson metal-insulator transition [15]—can occur. To reveal these (potential) single-particle phases, Fig. 3 shows $\nu(0)$ for the qBM model evaluated with the kernel polynomial method (KPM) [34]. Fig. 3(a) shows the $\nu(0)$ landscape while $A_{1,2}$ vary. There are large lakes with $\nu(0) > 0$ separated by *filaments* where the DOS is strongly enhanced. The filaments connect the magic angles (red stars) of the monochromatic potentials; both filaments and lakes host multifractal wave functions (see below). Fig. 3(b-d) show particular cuts. In the regime close to the A_1 or A_2 axes away from the magic angles, the system remains semimetallic and $\nu(0) \rightarrow 0$. By contrast, $\nu(0)$ peaks at the filaments and either remains nonzero or vanishes with a nontrivial power-law between the filaments, see Sec. IV. In the regions of comparable A_1 and A_2 , between the filaments, $\nu(0)$ is generally nonzero; in fact, as we show below, the system exhibits SWQC behavior in these regions associated to class-CI surface states [23].

Both cutoff Λ and number of moiré unit cells F_n determine the momentum space lattice, which need to both be large; therefore, to determine wave functions, we employ the Chebyshev filtering and shaking method [35, 36]. This method obtains eigenfunctions in a small energy window, which could contain thousands of states near a

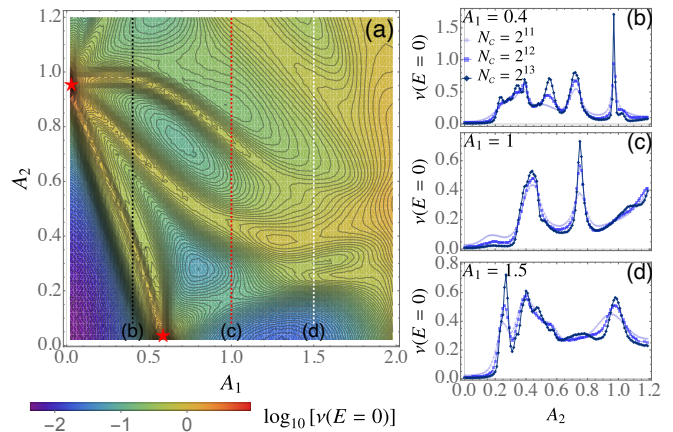


FIG. 3. The zero-energy density of states $\nu(0)$ for the qBM model in chiral limit. Here A_1 and A_2 are the strengths of the two sets of moiré potentials. (a): The map of $\nu(0)$ for the two moiré potentials. The zero-energy DOS has large peaks at the magic angles of the A_1 and A_2 potentials [indicated by red stars in (a)]. The magic angles of A_1 and A_2 are connected by several filaments, where $\nu(0)$ peaks. (b), (c) and (d): $\nu(0)$ along the cuts at $A_1 = 0.4$, 1 and 1.5, respectively. The peaks correspond to the filaments and $\nu(0)$ remains nonzero between these. This is our first hint that quasi-periodicity has driven a single-particle phase transition away from the semimetal in these regions. The data are obtained with KPM for a momentum lattice with $N_\Lambda = 17$ and $F_n = 89$. We use Chebyshev expansion order $N_c = 2^{11}$ for the DOS map (a) and $N_c = 2^{11}$, 2^{12} and 2^{13} in (b-d).

narrow band, see Sec. III C. We use the method to obtain eigenfunctions for the qBM model with $\sim 10^6$ lattice sites.

The statistics of single-particle wave functions can be characterized by the inverse participation ratio (IPR)

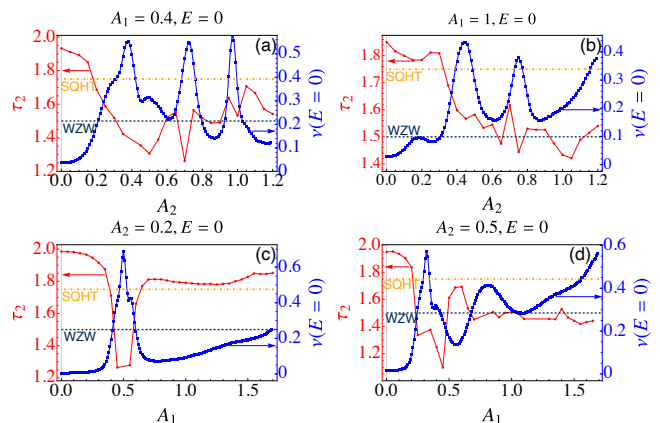


FIG. 4. The second multifractal dimension τ_2 averaged for states near zero energy and zero energy DOS $\nu(E = 0)$ for the qBM model. (a) and (b): along the vertical cuts at $A_1 = 0.4$ and 1, respectively; (c) and (d): along the horizontal cuts at $A_2 = 0.2$ and $A_2 = 0.5$, respectively. The navy blue dashed and orange dot-dashed lines indicate $\tau_2 = 3/2$ for the WZW states and $\tau_2 = 7/4$ for the SQHT states, respectively.

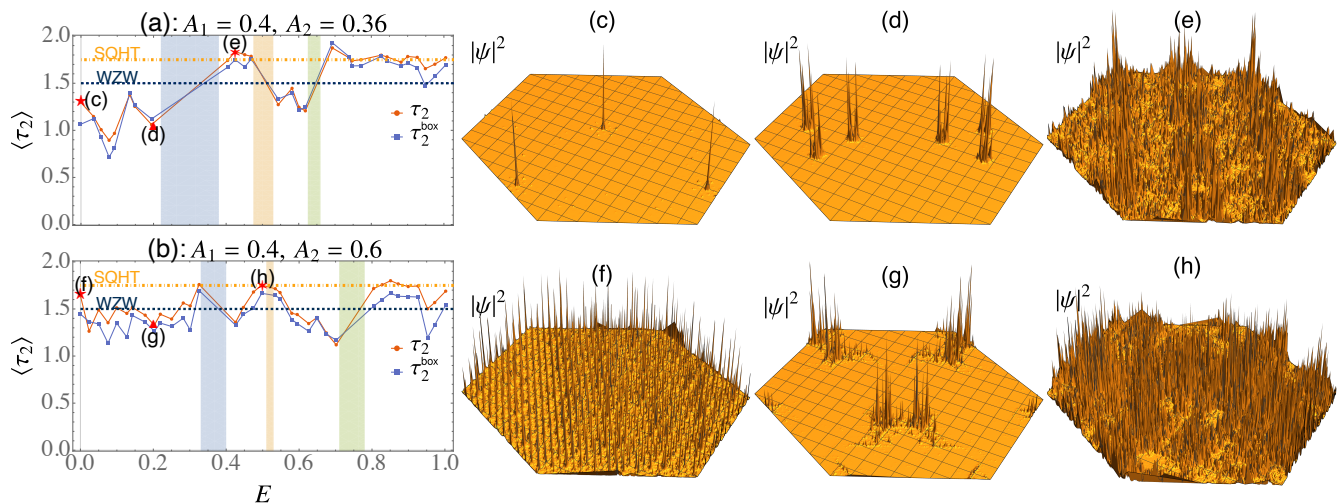


FIG. 5. The second multifractal dimension τ_2 versus energy and the wave functions at the one of filaments and in the lakes between the filaments. (a): τ_2 - E at the filament with $A_1 = 0.4$ and $A_2 = 0.36$; (b): same as (a) but in the lakes between filaments with $A_1 = 0.4$ and $A_2 = 0.6$. (c)-(e): the wave functions at the filament for states at $E = 0, 0.2$ and 0.425 ; (f)-(h): the wave functions in the lake for states at $E = 0, 0.2$ and 0.5 . The navy dashed and orange dot-dashed line in (a) and (b) show the reference value of τ_2 for the WZW and SQHT states, respectively. Here we $N_\Lambda = 11$, $F_n = 55$ and the wave functions reside on a 605×605 lattice in real space.

$P_q \equiv \sum_i |\psi_i|^{2q}$. Here ψ_i is the (normalized) wave function in real space, obtained by Fourier transform of the momentum-space wave function. For extended wave functions, $P_q \sim L^{-d(q-1)}$, with L the linear dimension of the system; for localized wave functions, $P_q \sim L^0$. Further, if $P_q \sim L^{-\tau_q}$ and $0 < \tau_q < d(q-1)$, that wave function is *critical*. In the thermodynamic limit ($L \rightarrow \infty$), the multifractal dimension can be evaluated via $\tau_q = -\log P_q / \log L$. The τ_q can also be obtained with the box-averaged IPR, $P_q^{\text{box}} = \sum_{i_b} \left(\sum_{\text{box}} |\psi_i|^2 \right)^q \propto b^{\tau_q}$, with b the linear size of the box. We use both methods to calculate the τ_q and they are consistent for the appropriate box sizes.

The second multifractal dimension τ_2 for low-energy wave functions is shown in Fig. 4 for the qBM model along the cuts $A_1 = 0.4$ and 1 . Corresponding τ_3 plots appear in Sec. IV. The value $\tau_2 \approx 2$ indicates ballistic wavefunctions, and Fig. 4(a) shows such states for small A_2 and $A_1 = 0.4$. We observe a correlation between $\nu(0)$ and multifractality; at the first filament (with increasing A_2), τ_2 decreases, fluctuates for stronger A_2 , and dips near the additional filaments. The value of τ_2 near the filaments in Fig. 4(a,c) indicates that the wave functions there are strongly multifractal, see also Fig. 5(c,d,g). Note that Fig. 4(c) follows the pattern for magic-angle semimetals as outlined in [13, 14]. In other regimes, such as between the filaments, the wave functions are also multifractal with a different value of τ_2 . In the nonperturbative regime, e.g., Fig. 4(b) along $A_1 = 1$, τ_2 fluctuates around $3/2$ and is only partially correlated with $\nu(0)$. However, at this point τ_2 appears to have saturated to the known value $\tau_2 = 3/2$ for zero-energy Wess-Zumino-Witten (WZW) surface states of a disordered class-CI TSC [15, 27, 30].

[Fig. 4(d) also shows this saturation.]

Finite-energy surface-state wave functions of a dirty TSC can also evade localization via SWQC, with critical statistics tied to a quantum-Hall plateau transition [23–25, 37]. For the class-CI qBM model, we anticipate finite-energy states with SWQC associated to the *spin* quantum-Hall transition (SQHT) [23, 24]. To compare with finite energies in the qBM model, we take two separate values, on the filament ($A_1 = 0.4$ and $A_2 = 0.36$) and between the filaments ($A_1 = 0.4$ and $A_2 = 0.6$) [see Fig. 5(a,b)], and examine a range of energies, extracting τ_2 . On the filament [Fig. 5(a)], the low-energy states are strongly multifractal (with $\tau_2 \approx 1$) with a few isolated peaks [energies $E = 0, 0.2$, Figs. 5(c,d)]; the higher energies oscillate between SQHT states [$\tau_2 \approx 7/4$ and less strongly peaked, see Fig. 5(e)] and strongly multifractal states. The filaments, originating from the flat bands at the magic-angles, have hybridized those states strongly into these multifractal states. In between the filaments [Fig. 5(b)], the low-energy wave functions are less multifractal than on the filament with WZW-like states [$\tau_2 \approx 3/2$ and $\tau_3 \approx 5/2$, Fig. 5(g)] and the high-energy states that reside deep within moiré bands are SQHT states [$\tau_2 \approx 7/4$ and $\tau_3 \approx 13/4$, Fig. 5(h)]. Near the energy gaps, the wave functions show stronger fractal features.

C. Superconductivity

With multifractality established and linked to the enhanced density of states, we are motivated by results that Cooper pairing amplitudes can be enhanced [18–22] to look at superconductivity in these regimes.

The Bogoliubov-de Gennes (BdG) Hamiltonian for the qBM model with pseudospin, layer, and spin-singlet s -wave pairing is given by $H = \int dr \chi^\dagger h_{\text{BdG}} \chi$. Here χ is the Nambu spinor spanning sublattice (σ), layer (τ), and particle-hole spaces (μ) and

$$h_{\text{BdG}} = h(\mathbf{r})\mu^3 + \Delta(\mathbf{r})\mu^1. \quad (2.3)$$

The Pauli matrices μ^i act on particle-hole space, and $h(\mathbf{r})$ is the qBM Hamiltonian in Eq. (2.1). The pairing amplitude $\Delta(\mathbf{r})$ is inhomogeneous due to quasiperiodicity and obtained self-consistently by decoupling a local attractive interaction with coupling strength U , as detailed in Sec. VI.

Fig. 6 shows the average Δ and its distribution function at half-filling obtained with KPM-based mean-field theory (Sec. III D). Figs. 6(a) and (b) plot the average order parameter Δ along the two cuts $A_1 = 0.4$ and 1, respectively. Without the A_2 potential, the interaction strength is below the critical one for 2D Dirac fermions [38–41] and Δ vanishes unless A_1 is close to the magic angles. Unlike the BM model, superconductivity in the qBM model is not fine-tuned and becomes nonzero as long as A_2 is not too weak. The strength of the superconductivity correlates with the change of the DOS at the Fermi energy, peaking near filaments with maximal DOS. However, the change in Δ is much shallower than that of the DOS. It results from the competition of the Fermi energy DOS and the spatial overlap of normal-state wave functions. In BCS theory, superconductivity benefits from a larger DOS at the Fermi energy. Here however, near the DOS peaks (the filaments), the spatial overlap of wave functions decays faster with energy difference than that in the lakes between filaments (not shown), which reduces the enhancement of superconductivity. Figs. 6(c) and (d) show the distribution of Δ_i and indicate that superconductivity is nonzero almost everywhere.

We compare Δ in the qBM and usual chiral BM models in Fig. 1. Fig. 1(b) shows Δ as a function of U in the qBM model for a particular $A_{1,2}$ choice. The scaling indicates *BCS-like* behavior $\Delta \sim \exp(-c/U)$, where c is a constant, in the $U \rightarrow 0$ limit. This should be contrasted with the chiral BM model, where $\Delta = 0$ identically for sufficiently small U away from the magic angle. In Sec. VI B, we show that *finite-energy* SQHT states (present due to SWQC) and critical DOS scaling for class CI implies BCS scaling.

Figs. 6(e) and (f) show the superfluid stiffness along the two cuts (computed with a double-KPM method explained in Sec. III E), which closely follows the analytical prediction $2\Delta/\pi$ for a clean Dirac superconductor [42]. This value can also be anticipated from the optical conductivity of a dirty s -wave superconductor, with imaginary part $\sigma_2(\omega) \simeq \pi \Delta \sigma_n/\omega$ [43]. Since the normal-state conductivity of the WZW Dirac model is $\sigma_n = 2e^2/\pi^2$, independent of disorder [15, 28], we get $\sigma_2(\omega) \simeq e^2 2\Delta/\pi\omega$. Superconductivity resists phase fluctuations and the transition temperature is determined by the strength of pairing amplitude. Localizing Althuler-Aronov effects have been found to suppress the stiffness in a quasiperiodic system

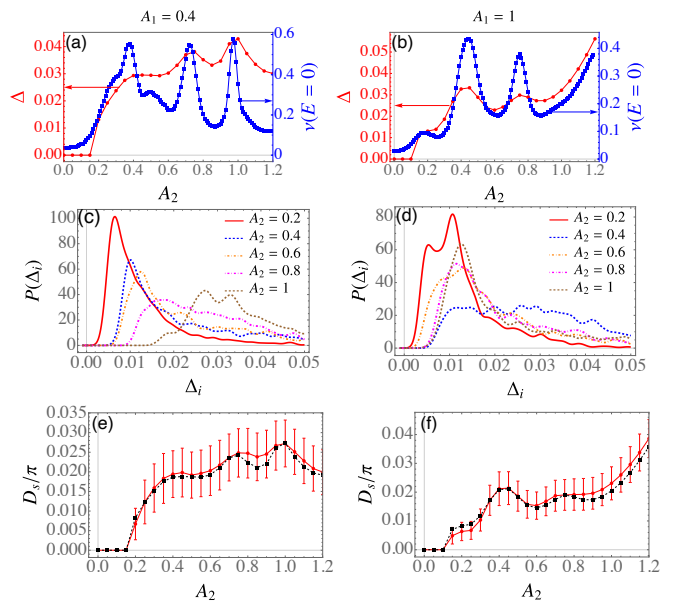


FIG. 6. The average superconductivity order parameter Δ , normal-state zero-energy DOS $\nu(0)$, distribution of the local order parameter Δ_i and superfluid stiffness. (a): Δ and $\nu(E=0)$ along the cut $A_1 = 0.4$; (b): same as (a) along the cut $A_1 = 1$; (c): the distribution of local order parameter Δ_i along $A_1 = 0.4$; (d) same as (c) along the cut $A_1 = 1$; (e): superfluid stiffness (red) along $A_1 = 0.4$ (clean limit value $2\Delta/\pi$ indicated by black dashed curve); (f): same as (e) along $A_1 = 1$. Here $U = 4v_F k_\theta$.

[22]; due to the effective topology these corrections are absent here [31].

D. Discussion

We have shown that the admixture of topology and quasiperiodicity in moiré materials can lead to remarkable quantum critical phenomena and robust superconductivity. Quasiperiodicity acts like disorder for strong mixing, but the coupling of same-valley Dirac fermions for small twists simulates topological surface states. Superconductivity is boosted without magic-angle fine tuning *and* without degrading the superfluid stiffness.

Taking this toy model seriously, it is worth pointing out that in the microscopic TBLG lattice, our pairing is formally Fulde–Ferrell–Larkin–Ovchinnikov, which would imply a pair-density wave on the lattice scale; further, it would be realized along with the pairing in the other valley to preserve time-reversal. However, the chiral, quasiperiodic BM model we use in Eq. (2.1) can be exactly constructed in a single layer of graphene with two mismatched $\sqrt{3}$ -potentials, as was shown for one such potential in Ref. [44]; in this system, pairing occurs between valleys (and is therefore, s -wave).

The qBM model is a toy version of TTLG, where we expect distinct multifractality will be found [32], as well as

in twisted bilayers with a superimposed, incommensurate superlattice. Topology plays an important role; while quasiperiodicity can drive transitions to critical states [45], it may not enhance and could even destroy superconductivity [46]. Nonetheless, this opens up the possibility for similar physics to occur in other moiré materials such as transition-metal dichalcogenide multilayers.

III. NUMERICAL METHOD FOR DOS, WAVE FUNCTIONS, AND SUPERCONDUCTIVITY

The two kinds of Chebyshev orthogonal polynomials are widely used to expand functions defined in the interval $[-1, 1]$. Physical quantities of a condensed matter system are usually expressed as functions of the bounded Hamiltonian, and are in principle well-suited to be expanded in terms of Chebyshev polynomials. However, the functions that determine many interesting physical properties such as the spectral and Green's functions are not smooth but have discontinuities or singularities. The truncated series expansion suffers from the so-called Gibbs phenomenon near discontinuities, where the expansion shows oscillation behavior. The Gibbs oscillation of a finite-series expansion cannot be resolved by simply increasing the degree of the expansion. As a resolution, various kernels are introduced to suppress the oscillation while keeping the series expansion positive and normalized. This is the idea of the so-called kernel polynomial method (KPM) [34]. Here we give a brief review of the KPM method, and related methods for wave functions, self-consistent mean-field theory, and superfluid stiffness.

A. Basics on Chebyshev polynomials and the kernel polynomial method

The Chebyshev polynomial of the first kind is most utilized in KPM, and its explicit expression is given by

$$T_n(x) = \cos(n \arccos x). \quad (3.1)$$

The polynomials can be obtained recursively with

$$T_0(x) = 1, \quad (3.2a)$$

$$T_1(x) = x, \quad (3.2b)$$

$$T_{n+1}(x) = 2xT_n(x) - T_{n-1}(x). \quad (3.2c)$$

A function $f(x)$ defined on the interval $x \in [-1, 1]$ can be expanded as

$$f(x) = \frac{1}{\pi\sqrt{1-x^2}} \left[\mu_0 + 2 \sum_{n=1}^{\infty} \mu_n T_n(x) \right], \quad (3.3)$$

$$\mu_n = \int_{-1}^1 f(x) T_n(x) dx. \quad (3.4)$$

The Gibbs oscillation of the Chebyshev expansion can be suppressed by introducing kernels

$$f(x) = \frac{1}{\pi\sqrt{1-x^2}} \left[\tilde{\mu}_0 + 2 \sum_{n=1}^{N_C-1} \tilde{\mu}_n T_n(x) \right], \quad (3.5a)$$

$$\tilde{\mu}_n = \mu_n g_n. \quad (3.5b)$$

Here N_C is the maximum degree of the Chebyshev polynomials, μ_n 's are the Chebyshev moments, and g_n 's are the kernel coefficients. The Jackson kernel is commonly employed and suitable for most applications,

$$g_n = \frac{1}{N_C + 1} \left[\begin{array}{l} (N_C - n + 1) \cos\left(\frac{\pi n}{N_C + 1}\right) \\ + \sin\left(\frac{\pi n}{N_C + 1}\right) \cot\left(\frac{\pi}{N_C + 1}\right) \end{array} \right]. \quad (3.6)$$

In practice, we can obtain $f(x)$ at discrete points using the discrete Fourier transform. For example, we can choose

$$x_k = \cos\left(\frac{k + \frac{1}{2}}{N_p} \pi\right), \quad k = 0, 1, \dots, N_p - 1. \quad (3.7)$$

Here N_p is the number of discrete points for x and we can choose $N_p \geq N_C$ to utilize all the available Chebyshev moments μ_n . Then we have

$$\gamma_k \equiv \pi \sqrt{1-x_k^2} f(x_k) = \tilde{\mu}_0 + 2 \sum_{n=1}^{N_C-1} \tilde{\mu}_n \cos\left[\frac{\pi n (k + \frac{1}{2})}{N_p}\right], \quad (3.8)$$

which can be obtained simultaneously with the fast-Fourier-transform algorithm. Another choice of x discretization is given by

$$x_k = \cos\left(\frac{k\pi}{N_p - 1}\right), \quad k = 0, 1, \dots, N_p - 1, \quad (3.9)$$

$$\gamma_k = \pi \sqrt{1-x_k^2} f(x_k) = \tilde{\mu}_0 + 2 \sum_{n=1}^{N_C-1} \tilde{\mu}_n \cos\left(\frac{\pi n k}{N_p - 1}\right). \quad (3.10)$$

The advantage of the second one is that it accesses $x_k = 0$ exactly with odd N_p , which is desired when we are interested in the scaling of the zero-energy DOS. The two choices of x_k corresponds to the two kinds of Chebyshev-Gauss quadrature in numerical integration of functions involving $f(x)$. With the first choice, we have

$$\int_{-1}^1 f(x) g(x) dx \approx \frac{1}{N_p} \sum_{k=0}^{N_p-1} \gamma_k g(x_k). \quad (3.11)$$

B. Density of states

The density of states of a system can be obtained with KPM efficiently. The global DOS of a system is given by

$$\rho(E) = \frac{1}{V} \sum_k \delta(E - E_k), \quad (3.12)$$

with V the volume of the system. Here and below, we let $|i\rangle$ and $|k\rangle$ denote the basis vectors in the position and energy bases, respectively. In general, the spectrum of a system is bounded by E_{\min} and E_{\max} , which can be obtained via the Lanczos algorithm. Then we can rescale the Hamiltonian,

$$\tilde{H} = aH + b, \quad (3.13)$$

with

$$a = \frac{2(1-\epsilon)}{E_{\max} - E_{\min}}, \quad (3.14)$$

$$b = -\frac{(1-\epsilon)(E_{\max} + E_{\min})}{E_{\max} - E_{\min}}, \quad (3.15)$$

with $0 < \epsilon \ll 1$ to guarantee the numerical stability. Thus we have

$$\rho(E) = \frac{a}{V} \sum_k \delta(\tilde{E} - \tilde{E}_k), \quad (3.16)$$

with $E = (\tilde{E} - b)/a$. The Chebyshev moments are then given by

$$\begin{aligned} \mu_n &= \int_{-1}^1 d\tilde{E} \rho(E) T_n(\tilde{E}) \\ &= \frac{a}{V} \sum_k T_n(\tilde{E}_k) = \frac{a}{V} \text{Tr} \left[T_n(\tilde{H}) \right]. \end{aligned} \quad (3.17)$$

The trace can be efficiently evaluated by averaging over a few independent random vectors,

$$\mu_n \approx \frac{a}{VR} \sum_{r=1}^R \langle \psi_r | T_n(\tilde{H}) | \psi_r \rangle. \quad (3.18)$$

Here R is the number of random vectors $\{\psi_{ri}\}$ satisfying

$$\langle \psi_{ri} \rangle = 0, \quad (3.19a)$$

$$\langle \psi_{ri} \psi_{r'j} \rangle = 0, \quad (3.19b)$$

$$\langle \psi_{ri}^* \psi_{r'j} \rangle = \delta_{rr'} \delta_{ij}. \quad (3.19c)$$

The angle brackets $\langle \dots \rangle$ denote the average over the ensemble of random vectors. ψ_{ri} is the i -th component of the r -th random vector, subject to some particular distribution. In our numerics, we use the uniform distribution for ψ_{ri} or the uniform distribution for θ with $\psi_{ri} = e^{i\theta}$. The vector $|\psi^n\rangle \equiv T_n(\tilde{H})|\psi\rangle$ can be obtained recursively using the relation in Eq. (3.2),

$$|\psi^0\rangle = T_0(\tilde{H})|\psi\rangle = |\psi\rangle, \quad (3.20a)$$

$$|\psi^1\rangle = T_1(\tilde{H})|\psi\rangle = \tilde{H}|\psi\rangle, \quad (3.20b)$$

\vdots

$$|\psi^{n+1}\rangle = T_{n+1}(\tilde{H})|\psi\rangle = 2\tilde{H}|\psi^n\rangle - |\psi^{n-1}\rangle. \quad (3.20c)$$

Using the product relation of Chebyshev polynomials,

$$2T_m(x)T_n(x) = T_{m+n}(x) + T_{m-n}(x). \quad (3.21)$$

Then we have

$$\mu_{2n} = \frac{2a}{V} \langle \psi^n | \psi^n \rangle - \mu_0, \quad (3.22)$$

$$\mu_{2n+1} = \frac{2a}{V} \langle \psi^{n+1} | \psi^n \rangle - \mu_1. \quad (3.23)$$

The global DOS can be obtained with discrete Fourier transform of $\tilde{\mu}_n = \mu_n g_n$. Typically, averaging a few (~ 10) random vectors is enough to evaluate the global DOS accurately for large enough systems. As a result, the computational effort required for calculating the global DOS is of the order of NN_C for a sparse Hamiltonian, with N denoting the dimension of the Hilbert space and N_C the degree of the Chebyshev polynomials.

C. Chebyshev filter methods for wave functions

1. Iterative filter method

Various numerical methods based on the KPM have been proposed to obtain the eigenvalues and eigenvectors of a large sparse matrix. One of them is the iterative Chebyshev filter diagonalization method proposed in Ref. [35]. The method aims to obtain the eigenvalue and eigenvectors in a small interval $[E_1, E_2]$. It starts with an ensemble of random vectors, whose dimension is greater than the number of states in the interval estimated from the DOS. At each step of the iteration, the vectors are filtered with the kernel polynomial expansion of a filter function. Then the set of filtered vectors are orthonormalized to obtain an orthonormal basis in the interval. The eigenvalues, eigenvectors and residual vectors are obtained with Rayleigh-Ritz method. The steps can be repeated until the residual of all the eigenpairs in the interval satisfy the preset criteria. Various filter functions can be used for the method. One of them is the rectangular function,

$$W(x) = \Theta(x - E_1) \Theta(E_2 - x). \quad (3.24)$$

A vector $|\psi\rangle$ can be filtered to amplify its components in the interval via

$$|\psi^F\rangle = \sum_{n=0}^{N_C} c_n g_n T(\tilde{H})|\psi\rangle. \quad (3.25)$$

Here g_n is the kernel and c_n is an expansion coefficient. The latter can be obtained exactly with

$$c_n = \frac{2 - \delta_{n0}}{\pi} \int_{-1}^1 \frac{W(\tilde{x}) T_n(\tilde{x})}{\sqrt{1 - \tilde{x}^2}} d\tilde{x}. \quad (3.26)$$

2. Filter and shake method

Instead of the iterative Chebyshev filter method, we use the filter and shake method proposed in Ref. [36] to evaluate the eigenvalues and eigenvectors in an interval. The method uses the so-called exponential semicircle filter to obtain a vector $|\psi_0\rangle$ with numerically vanishing overlap with eigenvalues outside of the interval. Then the vector is “shaken” by Chebyshev iteration to obtain a set of vectors, which are superpositions of eigenvectors in the desired interval. The eigenvalues, eigenvectors and residual vectors are then obtained via the Rayleigh-Ritz method using the orthonormal basis vectors.

The exponential semicircle filter exploits the fact that the Chebyshev polynomials $T_n(x)$ diverge exponentially with n when x is outside of the defining interval $[-1, 1]$. When $|x| > 1$, we have

$$\arccos x = \begin{cases} i \cosh^{-1} x & x > 1, \\ \pi - i \cosh^{-1} x & x < -1. \end{cases} \quad (3.27)$$

Thus, we have

$$\begin{aligned} T_n(x) &= \cos(n \arccos x) \\ &= \begin{cases} \cosh(n \cosh^{-1} x), & x > 1, \\ (-1)^n \cosh(n \cosh^{-1} x), & x < -1. \end{cases} \end{aligned} \quad (3.28)$$

Using $\cosh^{-1}(1+x) \approx \sqrt{2x}$ with $x > 0$, we have

$$|T_n(x)| \sim \frac{1}{2} e^{n\sqrt{2(|x|-1)}},$$

with $|x| > 1$ and $n\sqrt{2(|x|-1)} \gg 1$. We can see that $|T_n(x)|$ grows exponentially with the degree of Chebyshev iteration when $|x| > 1$, while $|T_n(x)| \ll 1$ for $|x| < 1$. Therefore, the Chebyshev iteration itself provides an efficient filter by projecting the desired energy window out of the defining range of the Chebyshev polynomials.

Consider a system with Hamiltonian H and spectrum in the range $[E_{\min}, E_{\max}]$. We seek the eigenvalues and eigenstates in an energy window $[E_0 - \delta, E_0 + \delta]$. We can use a parabolic function $F(H)$ [see Fig. 7] to project the energy spectrum of H so that $F(E) > 1$ when $E \in [E_0 - \delta, E_0 + \delta]$ and $F(E) < 1$ when $E \notin [E_0 - \delta, E_0 + \delta]$. The parabolic function $F(x)$ is given by

$$\begin{aligned} F(H) &= a^2 (H - E_0)^2 - c^2 \\ &= [a(H - E_0) + c][a(H - E_0) - c], \end{aligned} \quad (3.29a)$$

$$a = \sqrt{\frac{2-\epsilon}{\mathcal{E}^2 - \delta^2}}, \quad c = \sqrt{\frac{(2-\epsilon)\delta^2}{\mathcal{E}^2 - \delta^2} + 1}, \quad (3.29b)$$

$$\mathcal{E} = \max\{|E_{\min} - E_0|, |E_{\max} - E_0|\}. \quad (3.29c)$$

Performing Chebyshev iteration on $F(H)$ on a random state $|\psi\rangle$, we have

$$|\psi^0\rangle = |\psi\rangle, \quad (3.30a)$$

$$|\psi^1\rangle = F(H) |\psi^0\rangle, \quad (3.30b)$$

...

$$|\psi^n\rangle = 2F(H) |\psi^n\rangle - |\psi^{n-1}\rangle. \quad (3.30c)$$

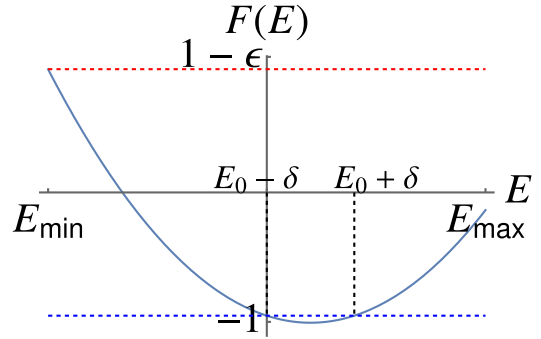


FIG. 7. Illustration of the exponential semicircle filter.

The initial random vector can be written as

$$|\psi\rangle = \sum_{m=1}^N c_m |m\rangle, \quad (3.31)$$

with $|m\rangle$ denoting the eigenstate of H with energy E_m and c_m a random number with $|c_m| \sim \frac{1}{\sqrt{N}}$. At order n of the Chebyshev iteration, we have

$$|\psi^n\rangle = \sum_m \tilde{c}_m |m\rangle, \quad (3.32a)$$

$$\tilde{c}_m = c_m T_n[F(E_m)]. \quad (3.32b)$$

When E_m falls out of the interval $[E_0 - \delta, E_0 + \delta]$, $T_n = \cos[n \arccos F(E_m)] \in [-1, 1]$ and \tilde{c}_m does not increase with the degree of Chebyshev expansion n . However, when $E_m \in [E_0 - \delta, E_0 + \delta]$, we have

$$\begin{aligned} T_n[F(E_m)] &= (-1)^n \cosh[n \cosh^{-1} F(E_m)] \\ &\approx (-1)^n \frac{1}{2} e^{n\sqrt{2[-a^2(E_m - E_0)^2 + c^2 - 1]}} \\ &= \frac{(-1)^n}{2} e^{\frac{2n}{\sqrt{\mathcal{E}^2 - \delta^2}} \sqrt{\delta^2 - (E_m - E_0)^2}}. \end{aligned} \quad (3.33)$$

Thus \tilde{c}_m grows as the exponential of a semicircle when $E_m \in [E_0 - \delta, E_0 + \delta]$ and n is large. Focusing on the interval within the half-width of the semi-circle, we have

$$\left| \frac{\tilde{c}_m}{c_m} \right| > \frac{1}{2} e^{\frac{n\delta}{\mathcal{E}}}. \quad (3.34)$$

It turns out that the exponential semicircle filter is much more efficient than the rectangular one and it can be used to accelerate the iterative method in Sec. III C 1. Moreover, Ref. [36] proposed that a complete basis for the states in the desired interval can be obtained by shaking the filtered state with Chebyshev iteration. In numerics, a double-precision float number has about 16 significant figures. When $n > \frac{\mathcal{E}}{\delta} \log(10^{16})$, the $|\psi^n\rangle$ contains numerically vanishing components of eigenstates outside of the desired interval and

$$|\psi^n\rangle \approx \sum_{E_0 - \delta < E_m < E_0 + \delta} \tilde{c}_m |m\rangle. \quad (3.35)$$

Now we take Chebyshev iteration with scaled Hamiltonian \tilde{H} and $|\psi^n\rangle$ as initial state. We have

$$|\phi^0\rangle = |\psi^n\rangle, \quad (3.36a)$$

$$|\phi^1\rangle = \tilde{H} |\phi^0\rangle, \quad (3.36b)$$

...

$$|\phi^{l+1}\rangle = 2\tilde{H} |\phi^l\rangle - |\phi^{l-1}\rangle. \quad (3.36c)$$

Then

$$|\phi^l\rangle \approx \sum_{E_0 - \delta < E_m < E_0 + \delta} \tilde{c}_m \cos\left(l \arccos \tilde{E}_m\right) |m\rangle. \quad (3.37)$$

Thus the amplitude of $|m\rangle$ in the $|\phi^l\rangle$ oscillates with its energy and the phase is given by

$$l \arccos \tilde{E}_m \approx l \arccos \tilde{E}_0 - \frac{l(\tilde{E}_m - \tilde{E}_0)}{\sqrt{1 - \tilde{E}_0^2}}, \quad (3.38)$$

with $|\tilde{E}_m - \tilde{E}_0| \ll 1$. The phases of the states in the desired interval now distribute across the interval $l \arccos \tilde{E}_0 - \frac{l}{\sqrt{1 - \tilde{E}_0^2}} [-\tilde{\delta}, \tilde{\delta}]$ with $\tilde{\delta} \ll 1$. When $l\tilde{\delta}/\sqrt{1 - \tilde{E}_0^2} \approx \frac{\pi}{2} \pmod{\pi}$, the phases of the all the states in the desired interval runs across an interval of length π . If the energies of the states uniformly distributed in the desired interval, the phases are also uniformed distributed in the length π interval around $l\pi/2$ if $\tilde{E}_0 \approx 0$. Thus for each l , we have a different superposition of eigenstates in the desired interval. Thus we can keep one state $|\phi^l\rangle$ for the basis for every $\lfloor \frac{\pi\sqrt{1 - \tilde{E}_0^2}}{2\tilde{\delta}} \rfloor$ Chebyshev iteration. Moreover, observing that $\arccos \tilde{E}_m \approx \frac{\pi}{2} + \tilde{E}$ when $\tilde{E}_m \approx 0$ and we have

$$\begin{aligned} \cos\left(l \arccos \tilde{E}_m\right) &\approx \cos\left(\frac{\pi l}{2} + l\tilde{E}\right) \\ &= \begin{cases} (-1)^{\frac{l}{2}} \cos(l\tilde{E}) & l \in \text{even}, \\ (-1)^{\frac{l+1}{2}} \sin(l\tilde{E}) & l \in \text{odd}. \end{cases} \end{aligned} \quad (3.39)$$

Thus we can keep both $|\phi^l\rangle$ and $|\phi^{l+1}\rangle$ in the basis when $l = \lfloor \frac{j\pi\tilde{\delta}}{2\tilde{\delta}} \rfloor$. Shaking $|\psi^n\rangle$ with Chebyshev iteration, we can generate a basis for the states in the desired interval. The eigenvalue and eigenstates can then be generated with this basis via the Rayleigh-Ritz method.

Now we summarize the filter and shake method as follows:

1. Calculate E_{\min} and E_{\max} of H with the Lanczos method.
2. Calculate the DOS of the system using KPM and estimate the number of states N_T in the desired interval $[E_0 - \delta, E_0 + \delta]$.

3. Generate the filtered state $|\psi^n\rangle$ from a random state using the exponential semicircle filter and $n > \frac{\mathcal{E}}{\delta} \log(10^{16})$ with $\mathcal{E} = \max\{|E_{\min} - E_0|, |E_{\max} - E_0|\}$.
4. Shake $|\psi^n\rangle$ with Chebyshev iteration and $|\phi^0\rangle = |\psi^n\rangle$. Keep $|\phi^l\rangle$ and $|\phi^{l+1}\rangle$ to the basis with $\frac{l\tilde{\delta}}{\mathcal{E}} \approx \frac{\pi}{2}$ (assuming $E_0 \approx 0$) and construct a basis $\{\Phi_j\}$ containing $N_S > N_T$ states. $N_S = 1.5N_T$ or $N_S = 2N_T$ is usually sufficient.
5. Orthogonalize the set of basis vector $\{\Phi_j\}$ and obtain an orthonormal basis containing $N_B \leq N_S$ states. This can be done with the SVQB algorithm.
6. Calculate the eigenvalue, eigenvectors and residual vectors using the orthonormal basis via Rayleigh-Ritz method.
7. Keep the states with $E \in [E_0 - \delta, E_0 + \delta]$ and residual smaller than the preset criteria η .

The method works best when the eigenvalues distribute uniformly across the desired interval. When there are degeneracies, we should generate a number of filtered states $|\psi^n\rangle$ with independent random initial vectors and generate a subset of the basis for each filtered state. When the number of filtered states is greater than the degeneracy of states in the interval, the filter and shake method works well. Moreover, the method is more efficient by using an appropriate number of filtered states, balancing the computational time for the filter step and the shake step.

D. Self-consistent BCS theory based on KPM

For an inhomogeneous system with interactions, mean-field order parameters also become inhomogeneous. The spatially varying order parameter generally prohibits analytical evaluation and exact diagonalization (ED) is often required to perform the calculation. However, it takes a lot of memory and computational time to diagonalize a large Hamiltonian matrix and the system size accessible is limited at the order of 10^4 lattice sites. The KPM based self-consistent mean field theory allows us to access larger systems with much less cost of memory and computational time.

1. Self-consistent BdG theory for a lattice model

Now we consider a lattice model with attractive Hubbard interaction,

$$H = -t \sum_{\langle ij \rangle \sigma} \left(c_{i\sigma}^\dagger c_{j\sigma} + H.c. \right) - U \sum_i n_{i\uparrow} n_{i\downarrow} - \mu \sum_i n_i. \quad (3.40)$$

It can be solved by the mean-field ansatz,

$$\Delta_i = -U \langle c_{i\downarrow} c_{i\uparrow} \rangle, \quad \langle n_{i\sigma} \rangle = \langle c_{i\sigma}^\dagger c_{i\sigma} \rangle = \frac{1}{2} \langle n \rangle. \quad (3.41)$$

The BdG mean-field Hamiltonian can be written as

$$H_{\text{eff}} = -t \sum_{\langle i,j \rangle \sigma} \left(c_{i\sigma}^\dagger c_{j\sigma} + H.c. \right) + \sum_i (V_i - \tilde{\mu}_i) n_{i\sigma} + \sum_i \left(\Delta_i c_{i\uparrow}^\dagger c_{i\downarrow}^\dagger + \Delta_i^* c_{i\uparrow} c_{i\downarrow} \right). \quad (3.42)$$

Here $\tilde{\mu} = \mu + U \langle n \rangle / 2$ incorporates the Hartree shift. H_{eff} can be diagonalized by the Bogoliubov transformation,

$$c_{i\uparrow} = \sum_n \left[u_n^i \alpha_n - (v_n^i)^* \beta_n^\dagger \right], \quad (3.43)$$

$$c_{i\downarrow} = \sum_n \left[(v_n^i)^* \alpha_n^\dagger + u_n^i \beta_n \right], \quad (3.44)$$

$$\begin{bmatrix} c_\uparrow \\ c_\downarrow^\dagger \end{bmatrix}^\top = \begin{bmatrix} u & -v^* \\ v & u^* \end{bmatrix} \begin{bmatrix} \alpha \\ (\beta^\dagger)^\top \end{bmatrix}, \quad (3.45)$$

with α and β^\dagger quasiparticle operators, α_i and β_i correspond to quasiparticles with the same energy and \sum' sums over all the positive energy states. u, v denote $N \times N$ matrices and $(u_{1n}, \dots, u_{Nn}, v_{1n}, \dots, v_{Nn})^\top$ is the n -th positive energy E_n eigenstate of the $2N \times 2N$ BdG Hamiltonian,

$$\begin{bmatrix} \hat{h}_0 & \Delta \\ \Delta^\dagger & -\hat{h}_0^\top \end{bmatrix} \begin{bmatrix} u_n \\ v_n \end{bmatrix} = E_n \begin{bmatrix} u_n \\ v_n \end{bmatrix}, \quad (3.46)$$

with $u_n = (u_{1n}, \dots, u_{Nn})^\top$ and $v_n = (v_{1n}, v_{2n}, \dots, v_{Nn})^\top$, $(\hat{h}_0)_{ij} = -t(\delta_{i,j+1} + \delta_{i+1,j}) - t(\delta_{i1}\delta_{jN} + \delta_{iN}\delta_{j1}) + (V_i - \tilde{\mu}_i)\delta_{ij}$ and $\Delta_{ij} = \Delta_i \delta_{ij}$. Thus we have

$$H_{\text{eff}} = \sum_n E_n (\alpha_n^\dagger \alpha_n - \beta_n \beta_n^\dagger). \quad (3.47)$$

The self-consistent conditions at $T = 0$ are then given by

$$\Delta_i = U \sum_n u_n^i (v_n^i)^*, \quad \langle n_i \rangle = 2 \sum_n |v_n^i|^2. \quad (3.48)$$

At finite temperature, we have

$$\begin{aligned} \Delta_i &= -U \langle c_{i\downarrow} c_{i\uparrow} \rangle \\ &= -U \sum_{mn} \left\langle \left[(v_m^i)^* \alpha_m^\dagger + u_m^i \beta_m \right] \left[u_n^i \alpha_n - (v_n^i)^* \beta_n^\dagger \right] \right\rangle \\ &= U \sum_n u_n^i (v_n^i)^* [1 - 2f(E_n)] \end{aligned} \quad (3.49)$$

and

$$\begin{aligned} \langle n_i \rangle &= \langle c_{i\uparrow}^\dagger c_{i\uparrow} \rangle + \langle c_{i\downarrow}^\dagger c_{i\downarrow} \rangle \\ &= 2 \sum_n \left[|u_n^i|^2 f(E_n) + |v_n^i|^2 (1 - f(E_n)) \right]. \end{aligned} \quad (3.50)$$

Here $f(E_n) = \frac{1}{e^{\beta E_n} + 1}$ is the Fermi distribution function for the quasiparticles with energy E_n .

It turns out to be convenient to write the eigenstates in the following form,

$$\begin{aligned} \begin{pmatrix} u & -v^* \\ v & u^* \end{pmatrix} &= \begin{pmatrix} u_1^i & \cdots & u_N^i & - (v_1^i)^* & \cdots & - (v_N^i)^* \\ v_1^i & \cdots & v_N^i & (u_1^i)^* & \cdots & (u_N^i)^* \end{pmatrix} \\ &= \begin{pmatrix} u_1^i & \cdots & u_N^i & u_{-1}^i & \cdots & u_{-N}^i \\ v_1^i & \cdots & v_N^i & v_{-1}^i & \cdots & v_{-N}^i \end{pmatrix}, \end{aligned} \quad (3.51)$$

with the first N columns for the N positive energy states and the last N columns for the negative energy states. Denote the eigenstate matrix as

$$\begin{pmatrix} u_1^i & \cdots & u_N^i & u_{-1}^i & \cdots & u_{-N}^i \\ v_1^i & \cdots & v_N^i & v_{-1}^i & \cdots & v_{-N}^i \end{pmatrix}, \quad (3.52)$$

with $u_{-n}^i = - (v_n^i)^*$ and $v_{-n}^i = (u_n^i)^*$. Here

$$\begin{aligned} u_n^i &= \langle i \uparrow | n \rangle, \quad v_n = \langle i \downarrow | n \rangle, \quad 1 \leq i \leq N, \\ & \quad -N \leq n \leq N, \quad n \neq 0. \end{aligned} \quad (3.53)$$

Here $|i \uparrow\rangle = c_{i\uparrow}^\dagger |0\rangle$ and $|i \downarrow\rangle = c_{i\downarrow} |0\rangle$ with $|0\rangle$ being the BCS ground state without quasiparticle excitations. The corresponding Bogoliubov transformation is given by

$$c_{i\uparrow} = \sum_n \left(u_n^i \alpha_n + u_{-n}^i \alpha_{-n}^\dagger \right), \quad (3.54)$$

$$c_{i\downarrow} = \sum_n \left[(v_n^i)^* \alpha_n^\dagger + (v_{-n}^i)^* \alpha_{-n} \right], \quad (3.55)$$

$$\begin{bmatrix} c_\uparrow \\ c_\downarrow^\dagger \end{bmatrix}^\top = \begin{bmatrix} u_+ & u_- \\ v_+ & v_- \end{bmatrix} \begin{bmatrix} \alpha \\ (\alpha^\dagger)^\top \end{bmatrix}. \quad (3.56)$$

In summary, we have

$$\Delta_i = -U \sum_n u_n^i (v_n^i)^* f(E_n), \quad E_{-n} = -E_n, \quad (3.57a)$$

$$n_i = 2 \sum_n |u_n^i|^2 f(E_n), \quad (3.57b)$$

$$u_n^i = \langle i \uparrow | n \rangle, \quad v_n = \langle i \downarrow | n \rangle. \quad (3.57c)$$

These expressions for Δ_i and n_i are easier to implement at finite temperature and are suitable to be generalized to the KPM method.

2. KPM Implementation of the self-consistent BdG theory

The BdG Hamiltonian has particle-hole symmetry and its spectrum is symmetric with respect to 0. Thus we can rescale the BdG Hamiltonian with

$$\tilde{H} = aH, \quad a = \frac{1 - \epsilon}{|E_g|}, \quad (3.58)$$

with E_g being the smallest eigenenergy of the BdG Hamiltonian.

We define the pairing and density spectral functions,

$$\begin{aligned} \Delta_i(E) &= -U \sum_n u_n^i (v_n^i)^* \delta(E - E_n) \\ &= -U \sum_n \langle i \uparrow | n \rangle \langle n | i \downarrow \rangle \delta(E - E_n), \end{aligned} \quad (3.59)$$

$$\begin{aligned} \rho_i(E) &= 2 \sum_n |u_n^i|^2 \delta(E - E_n) \\ &= 2 \sum_n \langle i \uparrow | n \rangle \langle n | i \uparrow \rangle \delta(E - E_n). \end{aligned} \quad (3.60)$$

Therefore, the local pairing amplitude and local density can be obtained via

$$\Delta_i = \int dE \Delta_i(E) f(E), \quad (3.61)$$

$$n_i = \int dE \rho_i(E) f(E). \quad (3.62)$$

The rescaled spectral functions of the scaled Hamiltonian are given by

$$\begin{aligned} \tilde{\Delta}_i(\tilde{E}) &= -U \sum_n \langle i \uparrow | n \rangle \langle n | i \downarrow \rangle \delta(\tilde{E} - \tilde{E}_n) \\ &= \frac{1}{a} \Delta_i(E = a\tilde{E}), \end{aligned} \quad (3.63)$$

$$\begin{aligned} \tilde{\rho}_i(\tilde{E}) &= 2 \sum_n \langle i \uparrow | n \rangle \langle n | i \uparrow \rangle \delta(\tilde{E} - \tilde{E}_n) \\ &= \frac{1}{a} \rho_i(E = a\tilde{E}). \end{aligned} \quad (3.64)$$

The Chebyshev moments of the rescaled spectral functions are given by

$$\begin{aligned} \mu_m^{\Delta_i} &= \int_{-1}^1 \tilde{\Delta}_i(\tilde{E}) T_m(\tilde{E}) d\tilde{E} \\ &= -U \sum_n \langle i \uparrow | n \rangle \langle n | i \downarrow \rangle T_m(\tilde{E}_n) \\ &= -U \left(\langle i \downarrow | T_m(\tilde{H}) | i \uparrow \rangle \right)^*, \end{aligned} \quad (3.65)$$

$$\begin{aligned} \mu_m^{\rho_i} &= \int_{-1}^1 \tilde{\rho}_i(\tilde{E}) T_m(\tilde{E}) d\tilde{E} \\ &= 2 \sum_n \langle i \uparrow | n \rangle \langle n | i \uparrow \rangle T_m(\tilde{E}_n) \\ &= 2 \langle i \uparrow | T_m(\tilde{H}) | i \uparrow \rangle. \end{aligned} \quad (3.66)$$

The Chebyshev iteration can be performed starting with $|i \uparrow \rangle$,

$$|\psi_0 \rangle = |i \uparrow \rangle, \quad (3.67a)$$

$$|\psi_1 \rangle = \tilde{H} |\psi_0 \rangle, \quad (3.67b)$$

...

$$|\psi_{m+1} \rangle = 2\tilde{H} |\psi_m \rangle - |\psi_{m-1} \rangle. \quad (3.67c)$$

Thus we have the Chebyshev moments,

$$\mu_m^{\Delta_i} = -U \langle i \downarrow | \psi_m \rangle, \quad (3.68)$$

$$\mu_m^{\rho_i} = 2 \langle i \uparrow | \psi_m \rangle. \quad (3.69)$$

The Chebyshev moments can be obtained by reading spin up and down components of $|\psi_m \rangle$ without performing the inner product.

With N_C Chebyshev moments of Δ_i and μ_i available, we can evaluate the scaled spectral functions at points,

$$\tilde{E}_k = \cos \left[\frac{\pi \left(k + \frac{1}{2} \right)}{N_p} \right], \quad k = 0, 1, \dots, N_p - 1. \quad (3.70)$$

Usually we consider $N_p \geq N_C$ (e.g. $N_p = 2N_C$) and $\tilde{\Delta}_i(\tilde{E}_k)$ can be evaluated through the discrete cosine transform from the 1D array

$$\left\{ \tilde{\mu}_0, \tilde{\mu}_1, \dots, \tilde{\mu}_{N_p-1}, \underbrace{0, \dots, 0}_{N_p - N_C} \right\},$$

Then we have,

$$\begin{aligned} \gamma_k^{\Delta_i} &= \pi \sqrt{1 - \tilde{E}_k^2} \tilde{\Delta}_i(\tilde{E}_k) \\ &= \tilde{\mu}_0^{\Delta_i} + 2 \sum_{m=1}^{N_C-1} \tilde{\mu}_m^{\Delta_i} \cos \left[\frac{\pi n (k + 1/2)}{N_p} \right], \end{aligned} \quad (3.71)$$

$$\begin{aligned} \gamma_k^{\rho_i} &= \pi \sqrt{1 - \tilde{E}_k^2} \tilde{\rho}_i(\tilde{E}_k) \\ &= \tilde{\mu}_0^{\rho_i} + 2 \sum_{m=1}^{N_C-1} \tilde{\mu}_m^{\rho_i} \cos \left[\frac{\pi n (k + 1/2)}{N_p} \right]. \end{aligned} \quad (3.72)$$

Here

$$\tilde{\mu}_m = g_m \mu_m, \quad (3.73)$$

with g_m being the Jackson kernel in Eq. (3.6). The integrals involving $f(x)$ can be obtained via Chebyshev-Gauss quadrature,

$$\begin{aligned} \int_{-1}^1 f(x) g(x) dx &= \int_{-1}^1 dx \frac{\sqrt{1-x^2} f(x) g(x)}{\sqrt{1-x^2}} \\ &= \frac{1}{N_p} \sum_{k=0}^{N_p-1} \gamma_k g(x_k). \end{aligned} \quad (3.74)$$

Thus we have

$$\begin{aligned}\Delta_i &= \int_{-E_{\max}}^{E_{\max}} \Delta_i(E) f(E) dE \\ &= \int_{-1}^1 \tilde{\Delta}_i(\tilde{E}) f(\tilde{E}) d\tilde{E} = \frac{1}{N_p} \sum_{k=0}^{N_p-1} \gamma_k^{\Delta_i} f(E_k),\end{aligned}\quad (3.75)$$

$$\begin{aligned}n_i &= \int_{-E_{\max}}^{E_{\max}} \rho_i(E) f(E) dE = \int_{-1}^1 \tilde{\rho}_i(\tilde{E}) f(\tilde{E}) d\tilde{E} \\ &= \frac{1}{N_p} \sum_{k=0}^{N_p-1} \gamma_k^{\rho_i} f(E_k).\end{aligned}\quad (3.76)$$

Here $f(E_k)$ is the Fermi distribution function.

The self-consistent BdG theory can be performed until the difference of the output order parameters $\{\Delta_i, n_i\}$ are close enough to the input ones. At each iteration, Δ_i and n_i need to be evaluated site by site. The convergence of the iteration can be further accelerated by Broyden's method [47, 48]. The KPM-based method requires only a small amount of memory and computation effort that scales with $N^2 N_C$, with N being the number of lattice sites. On the other hand, the computational effort of ED scales with N^3 . On our test platform with 2 CPUs [Intel(R) Xeon(R) CPU E5-2650 v4 @ 2.20GHz], the KPM-based method surpasses the ED-based one when $N \approx 2000$ and $N_C = 4096$. Therefore, the KPM-based mean-field method is superior to ED-based one as long as we need to deal with systems with more than several thousand lattice sites. Moreover, the KPM-based method can be easily accelerated with a parallel computation scheme like MPI. The communication cost is very low and the acceleration scales linearly with the number of MPI processes. Thus, very large system sizes can be accessed with enough resources.

3. Continuum model with local interaction

For the qBM-BCS model, the Hamiltonian can be written as

$$H = \int d\mathbf{r} \chi^\dagger [h(\mathbf{r}) \mu^3 + \Delta(\mathbf{r}) \mu^1] \chi, \quad (3.77)$$

where $h(\mathbf{r})$ is the qBM one-body Hamiltonian from Eq. (2.1). Both terms are local in real space, but only the second term can be expressed as a sparse matrix in position space. The first term involves the Dirac operator $-i\boldsymbol{\sigma} \cdot \nabla$, which cannot be expressed as a short-range lattice Hamiltonian without introducing the fermion-doubling problem. Therefore, we work simultaneously with both real- and momentum-space lattices, switching back and forth as necessary. Starting with a real-space state $|\psi\rangle$, we have

$$H|\psi\rangle = H_2|\psi\rangle + \mathcal{F}^{-1}(H_1|\mathcal{F}\psi\rangle). \quad (3.78)$$

Here \mathcal{F} is the Fourier transform from real space to momentum space, and

$$H_1 = \int d\mathbf{r} \chi^\dagger h(\mathbf{r}) \mu^3 \chi = \int_{\mathbf{k}_1 \mathbf{k}_2} \chi_{\mathbf{k}_1}^\dagger \hat{h}_{\mathbf{k}_1 \mathbf{k}_2} \chi_{\mathbf{k}_2}, \quad (3.79)$$

$$H_2 = \int d\mathbf{r} \chi^\dagger \Delta(\mathbf{r}) \mu^1 \chi. \quad (3.80)$$

The Hamiltonian matrix of the first term is sparse in momentum space and the action of H_1 on the momentum space wave function $|\mathcal{F}\psi\rangle$ is cheap to calculate. On the other hand, the Hamiltonian matrix of the second term is sparse in real space, as it acts locally on the real-space wave function. With this procedure, we can deal with a system with Dirac cones exactly without involving the fermion-doubling problem. The most computational challenging part now lies on the Fourier transform of wave functions, which can be done by fast-Fourier algorithm provided in vendor software packages.

E. Calculation of superfluid stiffness with KPM

1. Superfluid stiffness of lattice model

Consider the monochromatic electromagnetic field with vector potential $\mathbf{A}(\mathbf{r}_i, t)$,

$$\mathbf{A}(\mathbf{r}_i, t) = \Re[\mathbf{A}(\omega, \mathbf{q}) e^{-i\omega t + i\mathbf{q} \cdot \mathbf{r}_i}], \quad \mathbf{E} = -\partial_t \mathbf{A}. \quad (3.81)$$

With Peierls substitution, the hopping terms are modified as

$$t_{ij} \rightarrow t_{ij} e^{ie\phi_{ij}}, \quad \phi_{ij} = A_x(\mathbf{r}_i, t)(x_i - x_j). \quad (3.82)$$

Here we assume the slowly-varying electric field is applied in x -direction and the hopping is short-ranged. Then the attractive Hubbard model under vector field is given by

$$H = H_0 - e \sum_i j_x^P(\mathbf{r}_i) A_x(\mathbf{r}_i) - \frac{e^2}{2} \sum_i A_x^2(\mathbf{r}_i) K_x(\mathbf{r}_i). \quad (3.83)$$

The paramagnetic current and kinetic-energy densities are

$$j_x^P(\mathbf{r}_i) = i \sum_{j\sigma} t_{ij} (x_i - x_j) c_{i\sigma}^\dagger c_{j\sigma}, \quad (3.84)$$

$$K_x(\mathbf{r}_i) = - \sum_{j\sigma} t_{ij} (x_i - x_j)^2 c_{i\sigma}^\dagger c_{j\sigma}. \quad (3.85)$$

The total current is given by

$$j_x(\mathbf{r}_i) = - \frac{\delta H}{\delta A_x(\mathbf{r}_i)} = e J_x^P(\mathbf{r}_i) + e^2 A_x(\mathbf{r}_i) K_x(\mathbf{r}_i). \quad (3.86)$$

With linear response theory, we have

$$J_x^P(\omega, \mathbf{q}) = -e \Pi_{xx}^R(\omega, \mathbf{q}) A_x(\omega, \mathbf{q}), \quad (3.87)$$

$$j_x(\omega, \mathbf{q}) = e^2 [-\Pi_{xx}^R(\omega, \mathbf{q}) + K_x] A_x(\omega, \mathbf{q}). \quad (3.88)$$

The superfluid stiffness is then given by [49]

$$\frac{D_s}{\pi e^2} = \Pi_{xx}^R(\omega = 0, q_x = 0, q_y \rightarrow 0) - \langle K_x \rangle. \quad (3.89)$$

It can be shown that the superfluid stiffness for the lattice model can be evaluated via

$$\frac{D_s}{\pi e^2} = -\Pi_{xx}^R(\omega = 0, q_x = 0, q_y \rightarrow 0) - \langle K_x \rangle, \quad (3.90a)$$

$$\Pi_{xx}^R(\omega, \mathbf{q}) = \frac{2}{V} \sum_{nm} \frac{f(E_n) - f(E_m)}{\omega + E_n - E_m + i\eta} \langle n | J_e^x(\mathbf{q}) | m \rangle \langle m | J^x(-\mathbf{q}) | n \rangle, \quad (3.90b)$$

$$\hat{J}_e^x(\mathbf{q}) = i \sum_{ij} e^{-i\mathbf{q}\cdot\mathbf{r}_i} t_{ij} (x_i - x_j) |i \uparrow\rangle \langle j \uparrow|, \quad (3.90c)$$

$$\hat{J}^x(\mathbf{q}) = i \sum_{ij} e^{-i\mathbf{q}\cdot\mathbf{r}_i} t_{ij} (x_i - x_j) |i \uparrow\rangle \langle j \uparrow| + i \sum_{ij} e^{-i\mathbf{q}\cdot\mathbf{r}_i} t_{ij} (x_i - x_j) |i \downarrow\rangle \langle j \downarrow|, \quad (3.90d)$$

$$\langle K_x \rangle = -\frac{2}{V} \sum_{ij} t_{ij} (x_i - x_j)^2 \sum_n (u_n^i)^* u_n^j f(E_n) = \sum_n \langle n | \hat{K}_x f(E_n) | n \rangle, \quad (3.90e)$$

$$\hat{K}_x = -\frac{2}{V} \sum_{ij} t_{ij} (x_i - x_j)^2 |i \uparrow\rangle \langle j \uparrow|. \quad (3.90f)$$

2. KPM implementation

We define the two-point spectral function,

$$\pi(\omega_1, \omega_2, \mathbf{q}) = \frac{2}{V} \sum_{nm} \langle n | \hat{J}_e^x(\mathbf{q}) | m \rangle \langle m | \hat{J}^x(-\mathbf{q}) | n \rangle \delta(\omega_1 - E_n) \delta(\omega_2 - E_m). \quad (3.91)$$

Then the rescaled spectral function can be expressed using the kernel polynomial method,

$$\tilde{\pi}(\omega_1, \omega_2) = \sum_{kl=0}^{N_C-1} \frac{\mu_{kl} h_{kl} g_k g_l T_k(\omega_1) T_l(\omega_2)}{\pi^2 \sqrt{(1-\omega_1^2)(1-\omega_2^2)}}. \quad (3.92)$$

Here $\tilde{\pi}$ stands for the function with argument rescaled to the interval $[-1, 1]$ and

$$h_{kl} = \frac{2}{1 + \delta_{k,0}} \frac{2}{1 + \delta_{l,0}}, \quad (3.93)$$

and g_k are the kernel damping factors. We use the Jackson kernel for the spectral function.

The moments are obtained with

$$\begin{aligned} \mu_{kl} &= \int_{-1}^1 d\omega_1 \int_{-1}^1 d\omega_2 \tilde{\pi}_{xx}(\omega_1, \omega_2) T_k(\omega_1) T_l(\omega_2) \\ &= \frac{2}{N} \sum_{nm} \langle n | \hat{J}_e^x(\mathbf{q}) | m \rangle \langle m | \hat{J}^x(-\mathbf{q}) | n \rangle T_k(\tilde{E}_n) T_l(\tilde{E}_m) \\ &= \frac{2}{V} \sum_{nm} \langle n | T_k(\tilde{H}) \hat{J}_e^x(\mathbf{q}) | m \rangle \langle m | T_l(\tilde{H}) \hat{J}^x(-\mathbf{q}) | n \rangle \\ &= \frac{2}{V} \text{Tr} \left[T_k(\tilde{H}) \hat{J}_e^x(\mathbf{q}) T_l(\tilde{H}) \hat{J}^x(-\mathbf{q}) \right]. \end{aligned} \quad (3.94)$$

The trace can be efficiently and accurately averaged over a small number of random vectors.

In practice, the evaluation of $\tilde{\Pi}_{xx}$ in Eq. (3.92) can be efficiently implemented with the help of the discrete FFT, similar to the one-point case. We would evaluate $\tilde{\Pi}_{xx}(\omega_1, \omega_2)$ at discrete points,

$$\begin{aligned} \omega_1 &= \omega_m = \cos \left[\frac{\pi(m+1/2)}{N_p} \right], \\ \omega_2 &= \omega_n = \cos \left[\frac{\pi(n+1/2)}{N_p} \right]. \end{aligned} \quad (3.95)$$

Here N_p is the number of points evaluated for the integral and a reasonable choice is $N_p = 2N_C$. Then we have

$$\begin{aligned} \gamma_{mn} &= \pi^2 \sqrt{(1-\omega_m^2)(1-\omega_n^2)} \tilde{\pi}(\omega_m, \omega_n) \\ &= \sum_{kl=0}^{N_C-1} \mu_{kl} h_{kl} g_k g_l \\ &\quad \times \cos \left[\frac{\pi k(m+\frac{1}{2})}{N_p} \right] \cos \left[\frac{\pi l(n+\frac{1}{2})}{N_p} \right]. \end{aligned} \quad (3.96)$$

The summation is actually the discrete Fourier transform of the 2D array $\tilde{\mu}_{kl} = \mu_{kl} g_k g_l$, and it can be efficiently

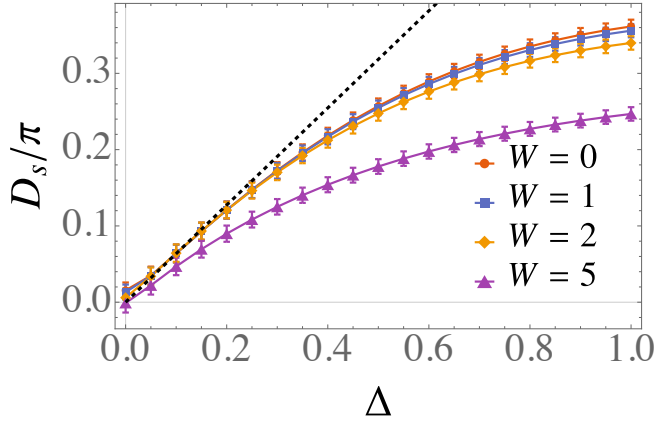


FIG. 8. Superfluid stiffness of a spin-singlet s -wave superconductor on the honeycomb lattice with uniform distributed on-site disorder potential $W_i \in [-\frac{W}{2}, \frac{W}{2}]$. The numerical data are evaluated on a honeycomb lattice with 100×100 unit cells and $N_C = 1024$. The dashed line shows the analytical prediction $\frac{D_s}{\pi} = \frac{2}{\pi}\Delta$ for a clean 2D Dirac superconductor.

evaluated via the fast-Fourier transform. Thus we have

$$\begin{aligned} \Pi_{xx}(\omega, \mathbf{q}) &= \int_{-1}^1 d\omega_1 \int_{-1}^1 d\omega_2 \frac{f(\omega_1) - f(\omega_2)}{\omega + \omega_1 - \omega_2 + i\eta} \tilde{\pi}(\omega_1, \omega_2) \\ &= \frac{1}{N_p^2} \sum_{mn=0}^{N_p-1} \gamma_{mn} \frac{f(\omega_n) - f(\omega_m)}{\omega + \omega_n - \omega_m + i\eta}. \end{aligned} \quad (3.97)$$

Here the integral is evaluated with the Gaussian quadrature.

For the kinetic energy term, we can defined the kinetic spectral function,

$$k_x(\omega) = \sum_n \langle n | \hat{K}_x | n \rangle \delta(\omega - E_n). \quad (3.98)$$

This term can also be evaluated with the KPM in the same fashion. At the end of the day, we would have

$$\langle K_x \rangle = \frac{1}{N_p} \sum_{m=0}^{N_p-1} \gamma_m f(\omega_m). \quad (3.99)$$

In Fig. 8, we show the superfluid stiffness of a Dirac superconductor on the honeycomb lattice with onsite disorder potential evaluated with the KPM. The superfluid stiffness D_s/π follows the analytical prediction $D_s/\pi = 2\Delta/\pi$ when the pairing amplitude is weak in the clean system. Interestingly, the superfluid stiffness is robust against a weak disorder potential and is only weakened by strong disorder.

3. Superfluid stiffness for Dirac superconductor

Now we consider Dirac superconductor with spin-singlet, layer-singlet, pseudospin-singlet pairing,

$$\begin{aligned} H &= \sum_{\mathbf{r}} c_{\mathbf{r}}^{\dagger} (-iv_F \boldsymbol{\sigma} \cdot \nabla) c_{\mathbf{r}} \\ &+ \Delta \sum_{\mathbf{r}} \left[ic_{\mathbf{r}\uparrow}^{\dagger} \sigma^2 \kappa^2 (c_{\mathbf{r}\downarrow}^{\dagger})^{\top} + \text{H.c.} \right]. \end{aligned} \quad (3.100)$$

Here $c_{\mathbf{r}}$ carries pseudospin (σ), layer (τ), and physical spin-1/2 (s) indices. Introducing the Nambu spinor

$$\chi = \begin{bmatrix} c_{\uparrow} \\ i\sigma^2 \kappa^2 (c_{\downarrow}^{\dagger})^{\top} \end{bmatrix}_{\mu}, \quad (3.101)$$

we have

$$H = \sum_{\mathbf{r}} \chi^{\dagger} \hat{h}_{\text{BdG}} \chi, \quad \hat{h}_{\text{BdG}} = (-iv_F \boldsymbol{\sigma} \cdot \nabla) \mu^3 + \Delta \mu^1. \quad (3.102)$$

Here μ^i is the Pauli matrix in the particle-hole sector. The electric current operator is then given by

$$\mathbf{J} = \chi^{\dagger} \boldsymbol{\sigma} \chi. \quad (3.103)$$

The current-current correlation function is then given by

$$\begin{aligned} \Pi_{xx}^R(\omega, \mathbf{q}) &= \frac{1}{V} \sum_{nm} \frac{f(E_n) - f(E_m)}{\omega + E_n - E_m + i\eta} \\ &\times \langle n | J_x(\mathbf{q}) | m \rangle \langle m | J_x(-\mathbf{q}) | n \rangle, \end{aligned} \quad (3.104)$$

which can be evaluated with KPM in the same fashion as the lattice model. However, unlike the lattice model, the diamagnetic term $\langle K_x \rangle$ vanishes in the expression for the superfluid stiffness and the paramagnetic current-current correlation functions diverges if no momentum cutoff is enforced. The superfluid stiffness should vanish when $\Delta = 0$, i.e. there is no Meissner effect for normal state. Therefore, we can regularize the current-current correlation function to obtain the physical superfluid stiffness via

$$\begin{aligned} \frac{D_s}{\pi} &= -\Pi_{xx}^R(\omega = 0, q_x = 0, q_y \rightarrow 0, \Delta \neq 0) \\ &+ \Pi_{xx}^R(\omega = 0, q_x = 0, q_y \rightarrow 0, \Delta = 0). \end{aligned} \quad (3.105)$$

IV. MORE DETAILS ON DOS AND CRITICAL STATES

A. System size scaling of multifractal wave function

Fig. 9 shows the second multifractal dimension τ_2 with different system sizes. It can be seen that τ_2 converges to the same value for increasing system sizes at most points, indicating that the critical wave functions in the qBM

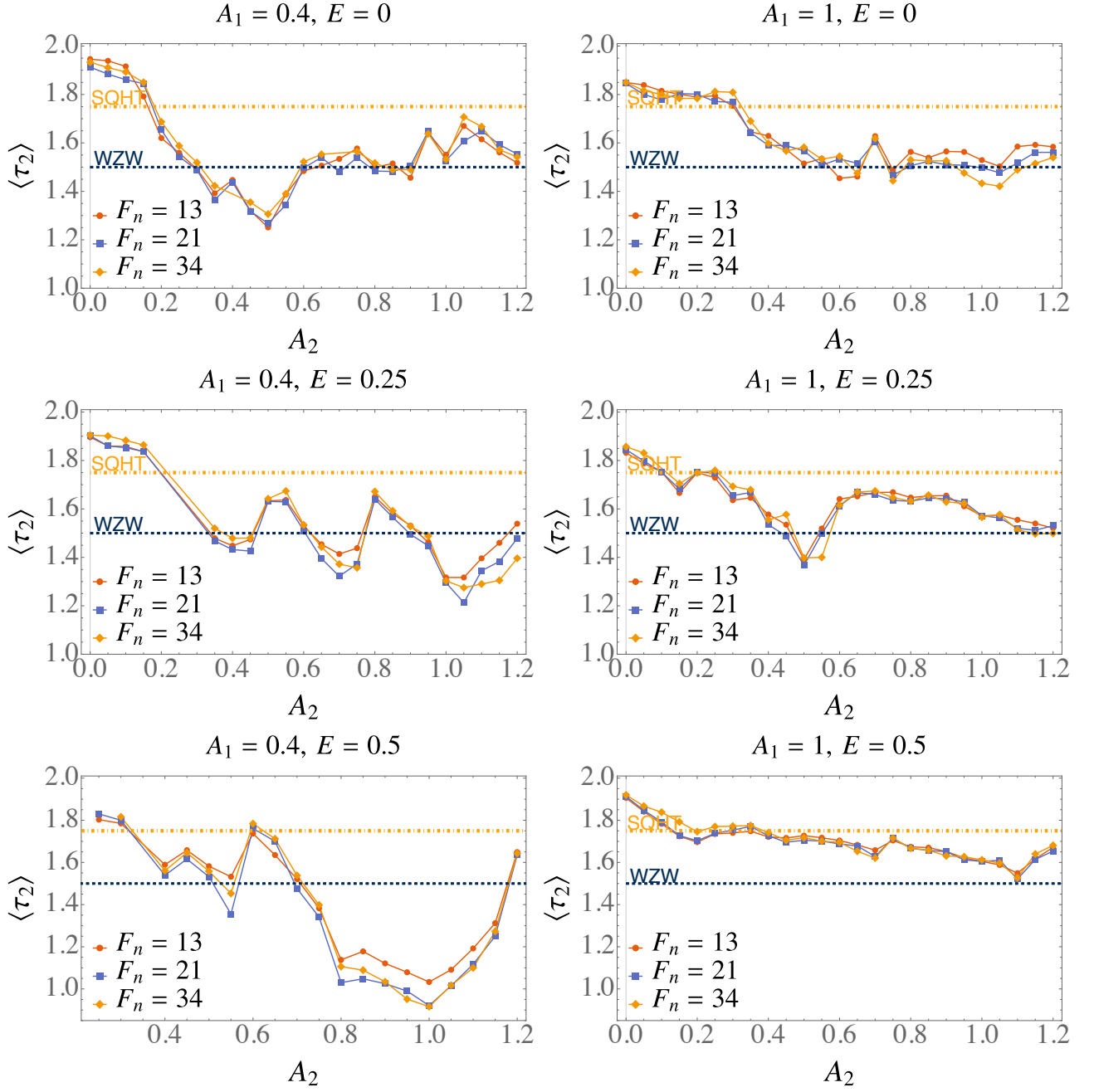


FIG. 9. The multifractal dimension τ_2 of wave functions at different energy with changing system size F_n along the two cuts $A_1 = 0.4$ and 1.

model are NOT a finite-size effect. There are several points where the τ_2 shows larger deviations for different system sizes. This occurs close to the filaments and the deviations can be attributed to the numerical errors when there are large number of states with similar energies (filaments).

B. DOS and multifractal properties in the lakes between filaments

The density of states of a system is given by

$$\rho(E) = \frac{1}{L} \sum_i \delta(E - \varepsilon_i), \quad (4.1)$$

with $\{\varepsilon_i\}$ denoting the set of eigenenergies. In the KPM [34], the Dirac delta functions are approximated by smooth functions. Using the Jackson kernel, these are

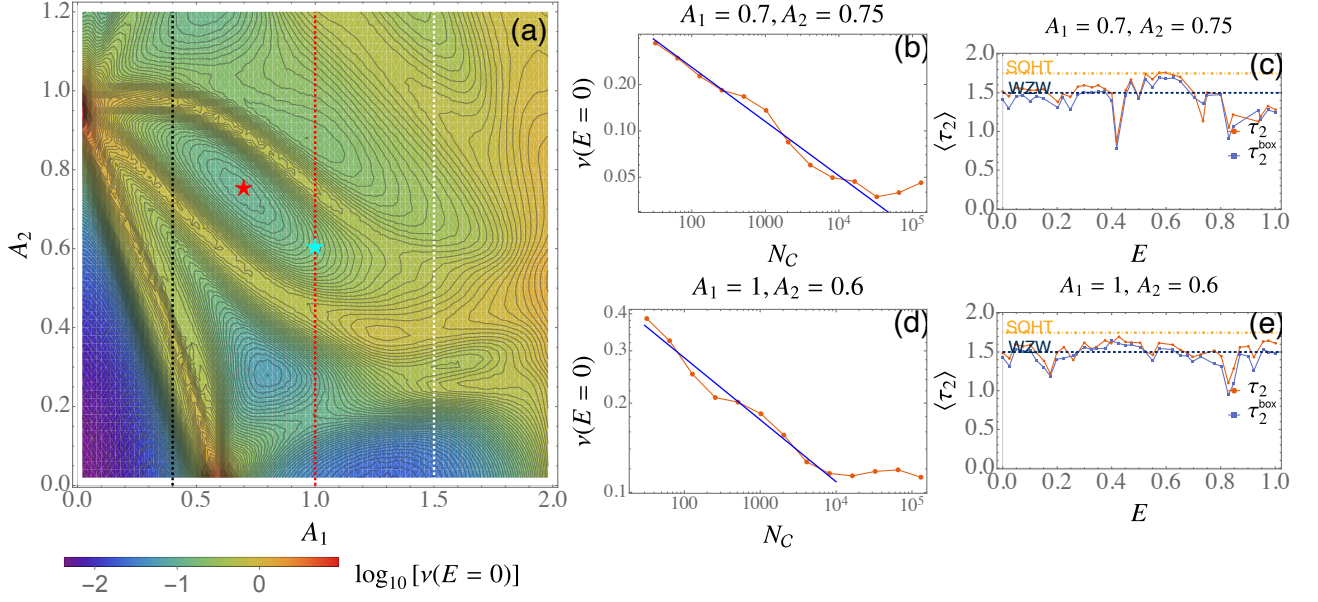


FIG. 10. The zero energy DOS $\nu(E=0)$, N_C scaling of $\nu(E=0)$ and multifractal dimension of wave functions in the lake of DOS map. In (b) and (d), we have $F_n = 233$ and $N_\Lambda = 15$ and the N_C dependence are fitted with $\sim N_C^{-0.352}$ and $\sim N_C^{-0.209}$, respectively.

Gaussians

$$\delta_{\text{KPM}}^J(x) \approx \frac{1}{\sqrt{2\pi\sigma^2}} \exp\left[-\frac{(x-a)^2}{2\sigma^2}\right]. \quad (4.2)$$

The variance

$$\sigma^2 = \left(\frac{\pi}{N_C}\right)^2 \left[1 - a^2 + \frac{3a^2 - 2}{N_C}\right]. \quad (4.3)$$

Here $-1 \leq a \leq 1$ and $\sigma = \pi/N_C$ at $a = 0$, $\sigma = \pi/N_C^{3/2}$ at $a = \pm 1$, with N_C being the order of the Chebyshev expansion.

Suppose we have a system whose density of states has power-law dependence on energy near $E = 0$,

$$\rho(E) \propto E^\alpha. \quad (4.4)$$

Then in the KPM with Jackson kernel, we have

$$\begin{aligned} \rho_{\text{KPM}}(E=0) &\approx \frac{1}{\sqrt{2\pi\sigma^2}} \int dE \rho(E) e^{-\frac{E^2}{2\sigma^2}} \\ &= \frac{1}{\sqrt{2\pi\sigma^2}} \int dE E^\alpha e^{-\frac{E^2}{2\sigma^2}} \\ &= \frac{\sigma^{\alpha+1}}{\sqrt{2\pi\sigma^2}} \int dx x^\alpha e^{-\frac{x^2}{2}} \propto \sigma^\alpha \sim N_C^{-\alpha}. \end{aligned} \quad (4.5)$$

The scaling behavior holds when N_C is not too small or too large. When N_C is too small, the higher-order corrections are significant and spoil the simple power-law scaling. When N_C is large enough that σ is at the order of level spacing of the system, the DOS resolves into isolated Gaussian peaks.

Fig. 10 shows the N_C scaling of the zero-energy DOS and multifractal dimensions of the wave functions at two points $A_1 = 0.7, A_2 = 0.75$ and $A_1 = 1, A_2 = 0.6$ in the lakes between the filaments. When N_C is not very large, the $\nu(E=0)$ has power-law dependence on N_C . It implies that the DOS near zero energy has power-law dependence on energy with $\nu(E) \sim |E|^{0.352}$ for $A_1 = 0.7, A_2 = 0.75$, and $\nu(E) \sim |E|^{0.209}$ for $A_1 = 1, A_2 = 0.6$, respectively.

C. The third multifractal dimension τ_3

In Figs. 4 and 5, we show the second multifractal dimension τ_2 for the qBM model. Fig. 11 shows the third multifractal dimension τ_3 .

V. SILVER RATIO QBM MODEL

The critical filaments and multifractal properties of wave functions are universal for the quasiperiodic Bistritzer-MacDonald model. In Secs. II and IV, we focus on the case $\mathbf{q}_i = \beta \mathbf{q}'_i$ with β the inverse golden ratio. In this section, we consider instead $\beta = 1/(\sqrt{2} + 1)$, which is the inverse silver ratio. The silver ratio can be approximately by P_{n+1}/P_n with $P_n = 1, 2, 5, 12, 29, 70, \dots$ the Pell numbers. Fig. 12 shows the zero-energy DOS map, and the second multifractal dimension τ_2 along two horizontal cuts $A_2 = 0.5$ and $A_2 = 1$ for the silver-ratio qBM model. There are filaments with large-zero energy DOS connecting the magic angle points of A_1 and A_2 . Between the filaments, the nonzero zero-energy DOS shows that

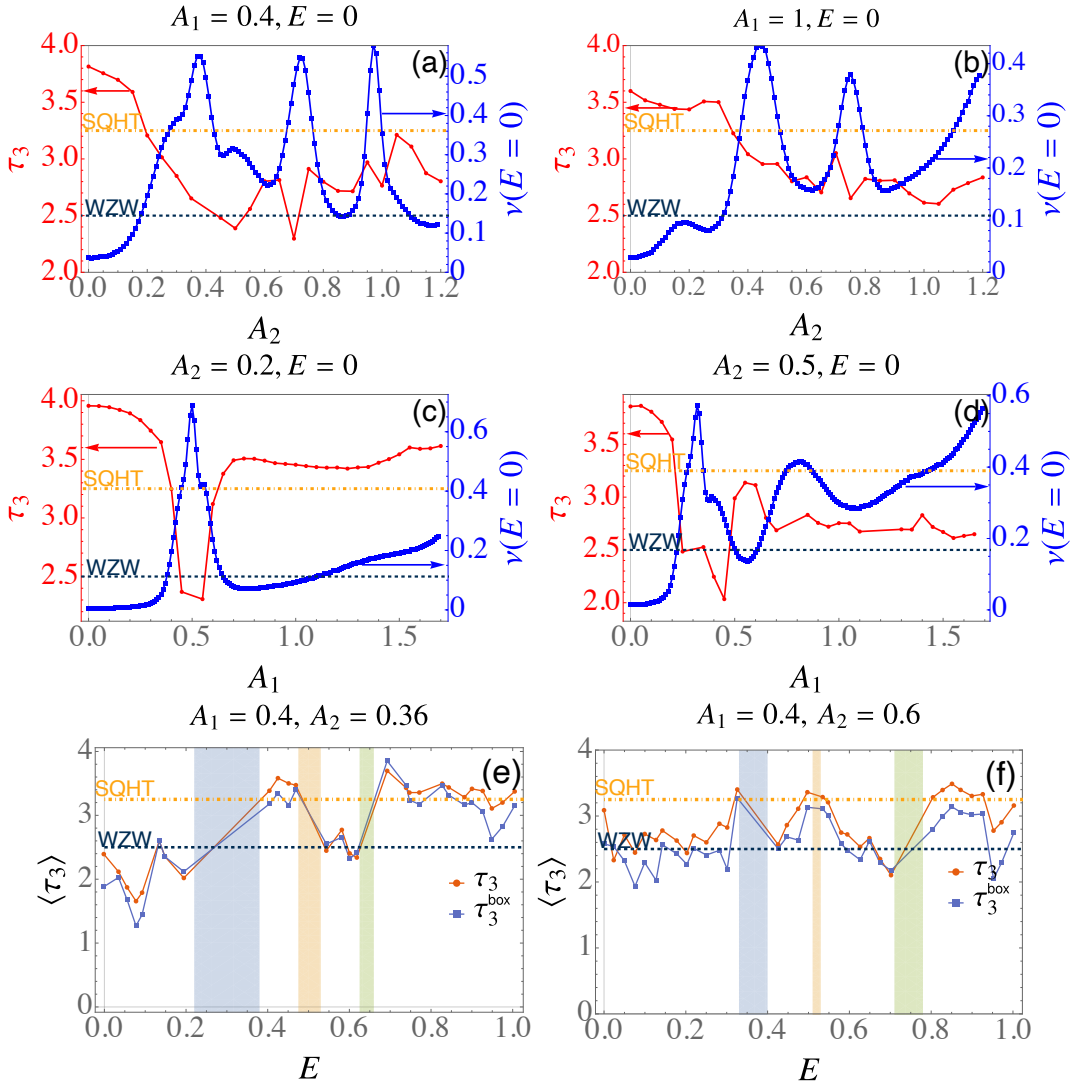


FIG. 11. The third multifractal dimension τ_3 averaged for states near zero energy (a)–(d) or finite energies (e), (f), along with the zero-energy DOS $\nu(E=0)$ for the golden-ratio qBM model. (a) and (b): along the vertical cuts at $A_1 = 0.4$ and 1 , respectively; (c) and (d) along the horizontal cuts at $A_2 = 0.2$ and 0.5 , respectively; (e) and (f) τ_3 versus energy for $A_1 = 0.4$ and $A_2 = 0.36$ (at a filament), $A_2 = 0.6$ (in the lake between filaments). The navy blue dashed and orange dot-dashed lines indicate $\tau_3 = 5/2$ for WZW states and $13/4$ for SQHT states, respectively [23].

the system is no longer semimetallic. At the filaments and in the lakes between the filaments, the wave functions near the zero energy become multifractal. The τ_2 is close to that of WZW state ($\tau_2 = 3/2$) for zero-energy wave functions in the lake along the cut $A_1 = 0.5$. In the lake along the $A_2 = 1$ cut, τ_2 is between that of WZW and SQHT states ($\tau_2 = 7/4$). At the filaments, τ_2 is smaller than $3/2$, indicating that these states are strongly multifractal. The results are very similar to the case of golden-ratio qBM model, indicating that our conclusions are general.

VI. MORE DETAILS ON THE SUPERCONDUCTIVITY

A. Numerical results

We consider superconductivity in the qBM model with a local pairing interaction,

$$H = \int d\mathbf{r} \psi^\dagger(\mathbf{r}) h(\mathbf{r}) \psi(\mathbf{r}) - U \int d\mathbf{r} \mathcal{B}^\dagger \mathcal{B}. \quad (6.1)$$

Here $h(\mathbf{r})$ is the qBM Hamiltonian given by Eq. (2.1), $\psi \rightarrow \psi_{\sigma,\tau,s}$ carries indices in sublattice (σ), layer (τ), and physical spin-1/2 (s) spaces, U gives the strength of the local attractive interaction, and \mathcal{B} is the bilinear for

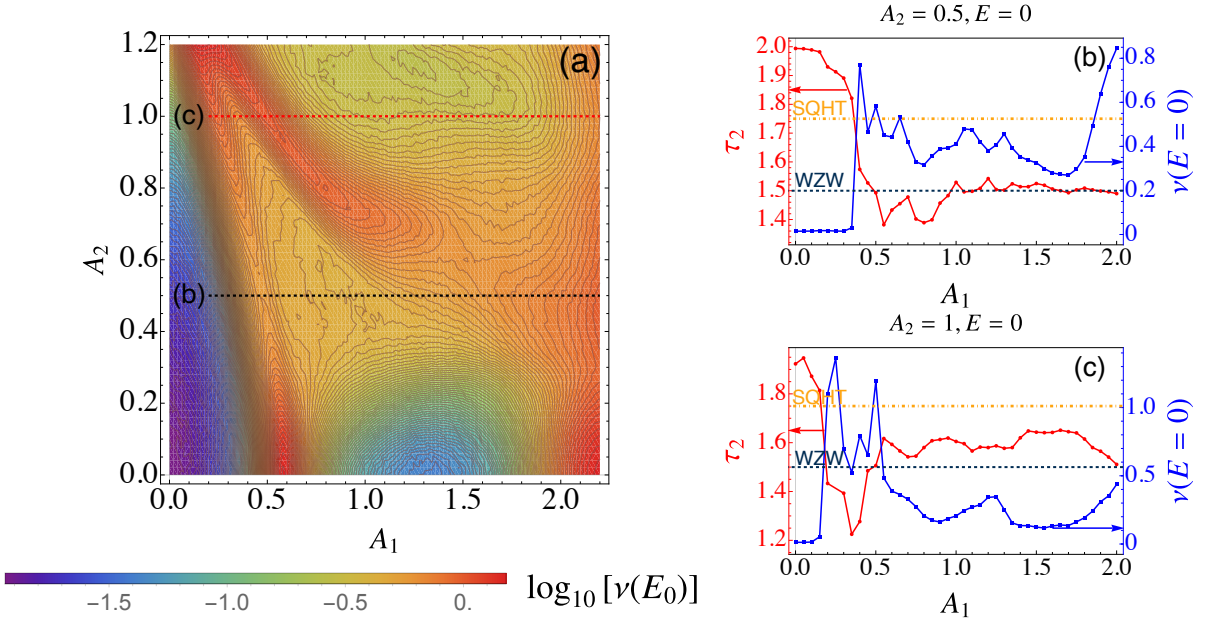


FIG. 12. Zero-energy DOS and the second multifractal dimension for the silver-ratio qBM model with $\mathbf{q}_i = \beta \mathbf{q}'_i$, with β a commensurate approximant to the inverse silver ratio $1/(\sqrt{2} + 1)$.

pseudospin-singlet, layer-singlet, and spin-singlet s -wave pairing

$$\mathcal{B} = \psi^\top \sigma^2 \tau^2 s^2 \psi. \quad (6.2)$$

The local interaction is well-known to be RG irrelevant for 2+1-D Dirac fermions and superconductivity only arises for an interaction strength comparable to the ultraviolet energy cutoff, see Eq. (6.18) below. In the presence of the usual Bistritzer-MacDonald (monochromatic) moiré potential, the low-energy spectrum remains linear and strong interactions are required for superconductivity, except in the close vicinity of the magic angle where a nearly flat band results in a much smaller critical interaction strength.

The attractive interaction can be decoupled with the mean-field ansatz,

$$\Delta(\mathbf{r}) = -U \langle \mathcal{B}(\mathbf{r}) \rangle. \quad (6.3)$$

Because we work with the quasiperiodic variant of the single-valley BM model, the s -wave pairing considered here would correspond to an FFLO state relative to the microscopic honeycomb lattices. We expect that the physics of pairing enhancement due to Chalker scaling of quantum-critical enhancement of wave functions [18, 19] and (approximate) topology-protected criticality will hold for interval-

ley pairing as well, but we leave this as a study for future work.

The mean-field Eqs. (2.3) and (6.3) are then readily solved self-consistently with the KPM based method. The KPM-based method allows us to deal with system sizes inaccessible with exact diagonalization. In Fig. 6, the data are obtained with the commensurate fraction denominator $F_n = 8$ and $N_\Lambda = 11$, and the dimension of the Hamiltonian matrix is 61952, which is very hard to diagonalize exactly even with the help of modern GPUs.

Fig. 13 shows the dependence of spatially averaged pairing amplitude $\langle \Delta \rangle$ on the system size and the degree of the kernel polynomials. We show the data with three system sizes $F_n = 5, 8$, and $F_n = 13$ with $N_\Lambda = 11$, which is solved on a triangular lattice with 55×55 , 88×88 and 143×143 sites, respectively. The $\langle \Delta \rangle$ only slightly changes with F_n . It indicates that the system size employed is large enough and the results apply for systems in thermodynamic limit. Fig. 13(b) show the N_C dependence of $\langle \Delta \rangle$ and the results converges when N_C is larger than 10^3 . In Fig. 6, we use $F_n = 8$, $N_\Lambda = 11$ and $N_C = 2048$.

B. Pairing of exact eigenstates approximation

Consider Dirac fermions with local attractive interactions and a spatially inhomogeneous potential,

$$H = \sum_{\mathbf{r}} c_{\mathbf{r}}^\dagger h(\mathbf{r}) c_{\mathbf{r}} - U \sum_{\mathbf{r}} \left[c_{\mathbf{r}\uparrow}^\dagger (-i\sigma^2 \tau^2) \left(c_{\mathbf{r}\downarrow}^\dagger \right)^\top \right] \left[(c_{\mathbf{r}\downarrow})^\top i\sigma^2 \tau^2 c_{\mathbf{r}\uparrow} \right]. \quad (6.4)$$

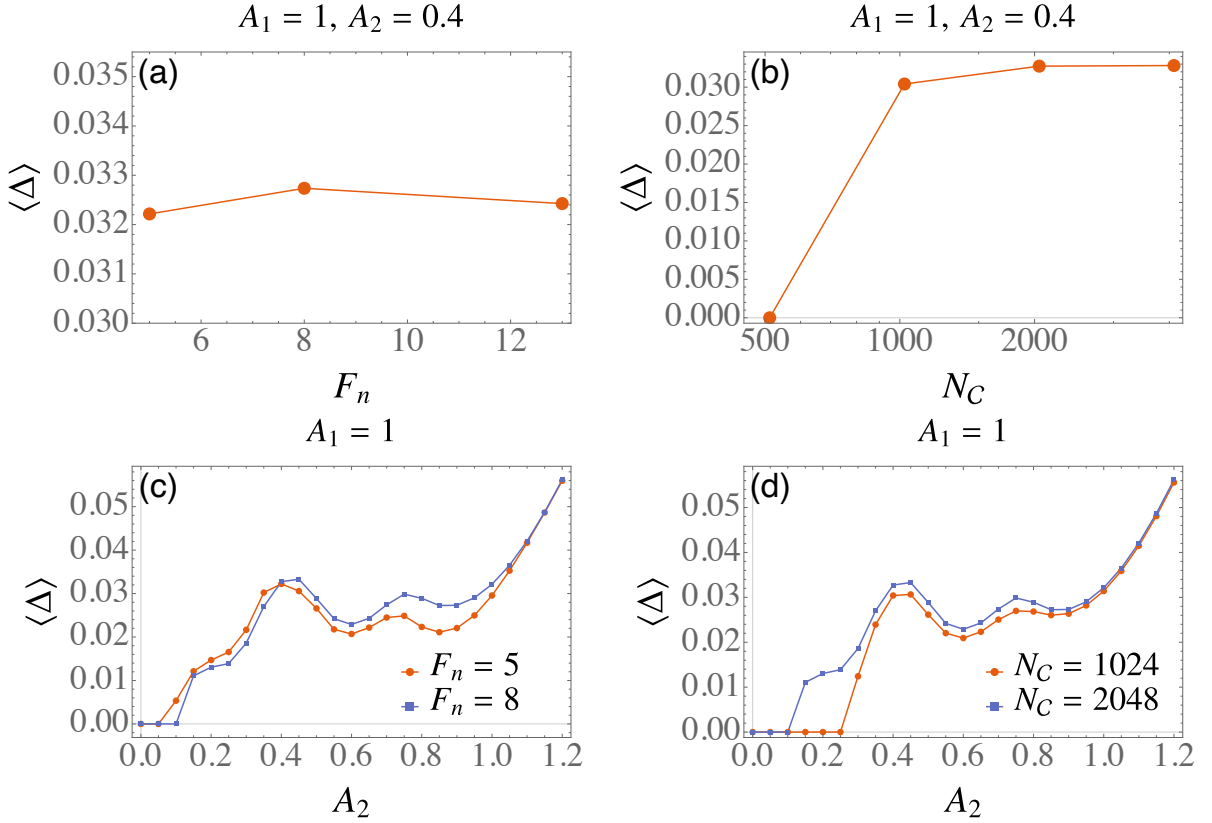


FIG. 13. The average pairing amplitude for qBM-BCS model with different system size and maximal degree of kernel polynomials N_C .

Here $c_{\mathbf{r}}$ carries pseudospin (σ), layer (τ) and spin (s) indices, and the one-body Dirac Hamiltonian $h(\mathbf{r})$ incorporates random or structured matrix potentials in some symmetry class, e.g. the class-CI chiral qBM model in Eq. (2.1). As in that case, we assume spin SU(2) and time-reversal symmetries in the normal state. Suppose the non-interacting part is solved by

$$h|\alpha\rangle = \varepsilon_{\alpha}|\alpha\rangle. \quad (6.5)$$

Then we have

$$c_{\mathbf{r}\sigma\tau s} = \sum_{\alpha} \langle \mathbf{r}\sigma\tau | \alpha \rangle a_{\alpha s} = \sum_{\alpha} \psi_{\alpha}(\mathbf{r}\sigma\tau) a_{\alpha s}. \quad (6.6)$$

Expressing the Eq. (6.4) in this basis gives

$$H = \sum_{\alpha, s} \varepsilon_{\alpha} a_{\alpha s}^{\dagger} a_{\alpha s} - U \sum_{\mathbf{r}} \sum_{\alpha\beta\gamma\delta} \left[\psi_{\alpha}^{\dagger}(\mathbf{r}) (-i\sigma^2\tau^2) \left(\psi_{\beta}^{\dagger}(\mathbf{r}) \right)^{\top} \psi_{\gamma}^{\top}(\mathbf{r}) (i\sigma^2\tau^2) \psi_{\delta}(\mathbf{r}) \right] a_{\alpha\uparrow}^{\dagger} a_{\beta\downarrow}^{\dagger} a_{\gamma\downarrow} a_{\delta\uparrow}. \quad (6.7)$$

The Cooper pairs are formed by pairing the time-reversal counterparts of spin-up and -down electrons. The time-reversed conjugate of $|\alpha\rangle$ is given by

$$|\bar{\alpha}\rangle = -i\sigma^2\tau^2|\alpha^*\rangle. \quad (6.8)$$

We neglect interactions in Eq. (6.7) except those responsible for creating such pairs. Thus we obtain the reduced BCS Hamiltonian

$$\begin{aligned} H_{\text{red}} &= \sum_{\alpha, s} \varepsilon_{\alpha} a_{\alpha s}^{\dagger} a_{\alpha s} - U \sum_{\alpha\beta} \left[\sum_{\mathbf{r}} \psi_{\alpha}^*(\mathbf{r}) (-i\sigma^2\tau^2) \psi_{\alpha}^*(\mathbf{r}) \psi_{\bar{\beta}}(\mathbf{r}) (i\sigma^2\tau^2) \psi_{\beta}(\mathbf{r}) \right] a_{\alpha\uparrow}^{\dagger} a_{\bar{\alpha}\downarrow}^{\dagger} a_{\bar{\beta}\downarrow} a_{\beta\uparrow} \\ &= \sum_{\alpha, s} \varepsilon_{\alpha} a_{\alpha s}^{\dagger} a_{\alpha s} - \sum_{\alpha\beta} M_{\alpha\beta} a_{\alpha\uparrow}^{\dagger} a_{\bar{\alpha}\downarrow}^{\dagger} a_{\bar{\beta}\downarrow} a_{\beta\uparrow}. \end{aligned} \quad (6.9)$$

Here

$$M_{\alpha\beta} = U \sum_{\mathbf{r}} |\psi_{\alpha}(\mathbf{r})|^2 |\psi_{\beta}(\mathbf{r})|^2, \quad (6.10)$$

where we have used

$$\psi_{\alpha} = -i\sigma^2 \tau^2 \psi_{\alpha}^*, \quad |\psi_{\alpha}(\mathbf{r})|^2 \equiv \sum_{\sigma\tau} |\psi_{\alpha}(\mathbf{r}\sigma\tau)|^2. \quad (6.11)$$

Then we have the mean-field gap equation,

$$\Delta_{\alpha} = \sum_{\lambda} M_{\alpha\lambda} \tanh\left(\frac{\beta\sqrt{\varepsilon_{\lambda}^2 + \Delta_{\lambda}^2}}{2}\right) \frac{\Delta_{\lambda}}{2\sqrt{\varepsilon_{\lambda}^2 + \Delta_{\lambda}^2}}. \quad (6.12)$$

In the *clean limit*, the wave functions are plane waves and the spatial overlap of wave functions at different energies is the same,

$$M_{\alpha\beta} \approx U \left(\frac{a}{L}\right)^d. \quad (6.13)$$

Here a is the lattice constant and L is the system size. The mean field gap equation is reduced to

$$\Delta_{\alpha} = U \sum_{\lambda} \left(\frac{a}{L}\right)^d \tanh\left(\frac{\beta\sqrt{\varepsilon_{\lambda}^2 + \Delta_{\lambda}^2}}{2}\right) \frac{\Delta_{\lambda}}{2\sqrt{\varepsilon_{\lambda}^2 + \Delta_{\lambda}^2}}. \quad (6.14)$$

Assuming that the pairing amplitude is energy independent, $\Delta(\varepsilon_{\alpha}) = \Delta$, we have

$$1 \approx U a^d \int_{-\Lambda}^{\Lambda} d\varepsilon \nu(\varepsilon) \tanh\left(\frac{\beta\sqrt{\varepsilon^2 + \Delta^2}}{2}\right) \frac{1}{2\sqrt{\varepsilon^2 + \Delta^2}}. \quad (6.15)$$

For Dirac fermions in 2D, the DOS is given by

$$\nu(\varepsilon) = \frac{1}{\pi v_F^2} |\varepsilon|. \quad (6.16)$$

Thus, we have the zero-temperature gap equation

$$\begin{aligned} \frac{2}{U} &= a^2 \int_{-\Lambda}^{\Lambda} d\varepsilon \frac{|\varepsilon|}{\pi v_F^2 \sqrt{\varepsilon^2 + \Delta^2}} \\ &= \frac{a^2}{\pi v_F^2} \left(\sqrt{\Lambda^2 + \Delta^2} - \Delta\right). \end{aligned} \quad (6.17)$$

Here Λ is the energy cutoff of the Dirac fermions. The equation has a solution for nonzero Δ only when the interaction strength is above the critical value

$$U_c = \frac{2\pi v_F^2}{\Lambda a^2} = \frac{2\Lambda}{\pi}, \quad (6.18)$$

where we have assumed that $\Lambda = v_F(\pi/a)$. Thus we obtain the well-known result that superconductivity only arises above the critical interaction strength for clean 2D Dirac fermions [38–42].

For *critical states*, the spatial overlap of the wave functions entering the matrix element is determined by Chalker scaling [24, 50, 51], and we have

$$M_{\alpha\beta} \sim U \mathbf{b} |\varepsilon_{\alpha} - \varepsilon_{\beta}|^{(\tau_2 - d)/z}. \quad (6.19)$$

Here z is the dynamical critical exponent of Dirac fermions with random or structural spatial inhomogeneity. The DOS of critical Dirac fermions near $\varepsilon = 0$ is modified by the disorder or quasiperiodic potential,

$$\nu(\varepsilon) \approx \mathbf{c} |\varepsilon|^{(d-z)/z}. \quad (6.20)$$

Thus we have the gap equation at $T = 0$,

$$\begin{aligned} 1 &= U \int_{-\Lambda}^{\Lambda} d\varepsilon \nu(\varepsilon) M_{\alpha\beta} \tanh\left(\frac{\beta\sqrt{\varepsilon^2 + \Delta^2}}{2}\right) \frac{1}{2\sqrt{\varepsilon^2 + \Delta^2}} \\ &\approx U \mathbf{a} \int_{-\Lambda}^{\Lambda} d\varepsilon |\varepsilon|^{\frac{\tau_2 - z}{z}} \tanh\left(\frac{\beta\sqrt{\varepsilon^2 + \Delta^2}}{2}\right) \frac{1}{2\sqrt{\varepsilon^2 + \Delta^2}}. \end{aligned} \quad (6.21)$$

Here $\mathbf{a} = \mathbf{b}\mathbf{c}$. For 2D disordered Dirac fermions in the chiral/WZNW version of class CI with winding number 2, we have [50]

$$z = \frac{7}{4} \quad (6.22)$$

If we further assume that, due to SWQC [23, 24], the appropriate wave-function fractal dimension is that of the class-C SQHT

$$d_2 \approx 7/4, \quad (6.23)$$

then we have

$$1 \approx U \mathbf{a} \int_{-\Lambda}^{\Lambda} d\varepsilon \tanh\left(\frac{\beta\sqrt{\varepsilon^2 + \Delta^2}}{2}\right) \frac{1}{2\sqrt{\varepsilon^2 + \Delta^2}}. \quad (6.24)$$

This is exactly the gap equation for a BCS superconductor of electrons with a Fermi surface if \mathbf{a} is replaced by the constant DOS at the Fermi level. At zero temperature, we have

$$\Delta = \frac{\Lambda}{\sinh\left(\frac{1}{U\mathbf{a}}\right)} \approx 2\Lambda e^{-1/(U\mathbf{a})}. \quad (6.25)$$

By contrast, if we instead employ the fractal dimension for low-energy WZNW wave functions $d_2 = 3/2$, we would get the non-BCS result if we neglect the UV cutoff [18, 19]

$$\Delta \propto U^{1/7}. \quad (6.26)$$

In both scenarios, the finite-threshold strength in the clean limit U_c [Eq. (6.18)] is lowered to zero for quantum-critical wave functions, *despite* the vanishing density-of-states for class CI $\nu(\varepsilon) \approx |\varepsilon|^{1/7}$.

The critical exponents in the qBM model deviate from the case of dirty Dirac fermions. But as is shown in Fig. 10, the DOS in the lake shows power-law dependence on energy. In Fig. 14, we show the dependence of the pairing amplitude on the interaction strength for Dirac fermions in the clean limit and in the critical lake of the chiral qBM model. In the clean limit, Δ becomes nonzero when U is above the critical interaction strength. In the lake with $A_1 = 1$ and $A_2 = 0.6$, the Δ vs. $1/U$ curve is approximately linear for weak interactions in the log-linear plot, which is consistent with the prediction in Eq. (6.25).

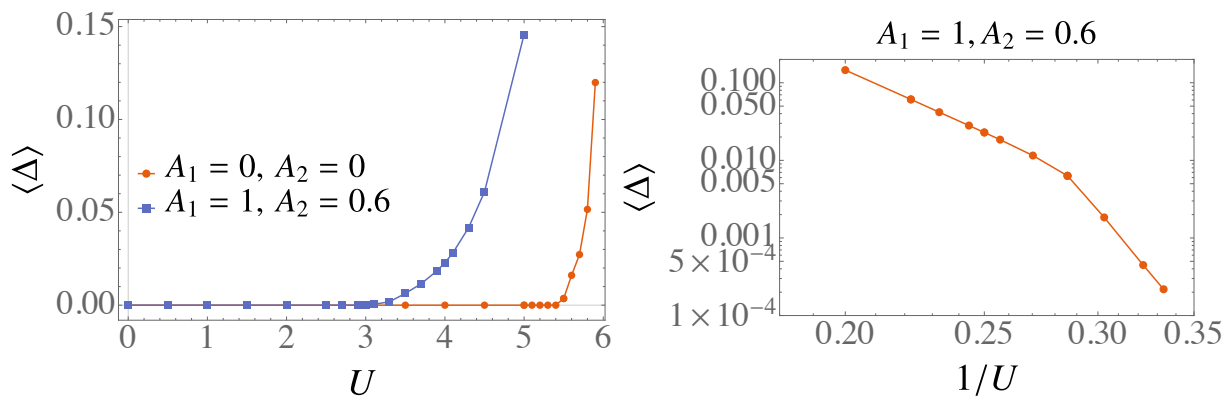


FIG. 14. The dependence of the pairing amplitude Δ on the interaction strength U for Dirac fermions in both the clean case and in the chiral qBM model.

ACKNOWLEDGMENTS

We thank S. Gopalakrishnan and E. König for helpful discussions. We further thank Aaron Dunbrack for pointing out the physical system that realizes our model. This work was supported by the Welch Foundation Grant No. C-1809 (X. Z. and M. S. F.) and by the National Science Foundation under Grant No. DMR-2238895 (J. H. W.). This work was performed in part

at Aspen Center for Physics, which is supported by NSF Grant No. PHY-2210452. This work was supported in part by the Big-Data Private-Cloud Research Cyberinfrastructure MRI-award funded by NSF under grant CNS-1338099 and by Rice University's Center for Research Computing (CRC). Portions of this research were conducted with high performance computing resources provided by Louisiana State University (<http://www.hpc.lsu.edu>).

-
- [1] For a review, see e.g. A. H. MacDonald, *Bilayer Graphene's Wicked, Twisted Road*, *Physics* **12**, 12 (2019).
- [2] J. M. B. Lopes dos Santos, N. M. R. Peres, and A. H. Castro Neto, *Graphene Bilayer with a Twist: Electronic Structure*, *Phys. Rev. Lett.* **99**, 256802 (2007).
- [3] Guohong Li, A. Luican, J. M. B. Lopes dos Santos, A. H. Castro Neto, A. Reina, J. Kong, and E. Y. Andrei, *Observation of Van Hove singularities in twisted graphene layers*, *Nature Phys* **6**, 109 (2010).
- [4] R. Bistritzer and A. H. MacDonald, *Moiré bands in twisted double-layer graphene*, *Proc. Natl. Acad. Sci. (USA)* **108**, 12233 (2011).
- [5] G. Tarnopolsky, A. J. Kruchkov, and A. Vishwanath, *Origin of Magic Angles in Twisted Bilayer Graphene*, *Phys. Rev. Lett.* **122**, 106405 (2019).
- [6] Z. Song, Z. Wang, W. Shi, G. Li, C. Fang, and B. A. Bernevig, *All Magic Angles in Twisted Bilayer Graphene are Topological*, *Phys. Rev. Lett.* **123**, 036401 (2019).
- [7] H. C. Po, L. Zou, A. Vishwanath, and T. Senthil, *Origin of Mott Insulating Behavior and Superconductivity in Twisted Bilayer Graphene*, *Phys. Rev. X* **8**, 031089 (2018).
- [8] H. C. Po, L. Zou, T. Senthil, and A. Vishwanath, *Faithful tight-binding models and fragile topology of magic-angle bilayer graphene*, *Phys. Rev. B* **99**, 195455 (2019).
- [9] J. Ahn, S. Park, and B.-J. Yang, *Failure of Nielsen-Ninomiya Theorem and Fragile Topology in Two-Dimensional Systems with Space-Time Inversion Symmetry: Application to Twisted Bilayer Graphene at Magic Angle*, *Phys. Rev. X* **9**, 021013 (2019).
- [10] A. Uri, S. C. de la Barrera, M. T. Randeria, *et al.*, *Superconductivity and strong interactions in a tunable moiré quasicrystal*, *Nature* **620**, 762 (2023).
- [11] Quasiperiodicity can also manifest due to the substrate, see X. Lai, D. Guerci, G. Li, K. Watanabe, T. Taniguchi, J. Wilson, J. H. Pixley, Eva Y. Andrei, *Imaging Self-aligned Moiré Crystals and Quasicrystals in Magic-angle Bilayer Graphene on hBN Heterostructures*, *arXiv: 2311.07819* (2023).
- [12] J. H. Pixley, J. H. Wilson, D. A. Huse, and S. Gopalakrishnan, *Weyl Semimetal to Metal Phase Transitions Driven by Quasiperiodic Potentials*, *Phys. Rev. Lett.* **120**, 207604 (2018).
- [13] Y.-Z. Chou, Y. Fu, J. H. Wilson, E. J. König, and J. H. Pixley, *Magic-angle semimetals with chiral symmetry*, *Phys. Rev. B* **101**, 235121 (2020).
- [14] Y. Fu, E. J. König, J. H. Wilson, Y.-Z. Chou, and J. H. Pixley, *Magic-angle semimetals*, *npj Quantum Mater.* **5**, 71 (2020).
- [15] F. Evers and A. D. Mirlin, *Anderson transitions*, *Rev. Mod. Phys.* **80**, 1355 (2008).
- [16] S. Aubry and G. André, *Analyticity breaking and Anderson localization in incommensurate lattices*, *Ann. Isr. Phys. Soc.* **3**, 133 (1980).
- [17] J. B. Sokoloff, *Unusual band structure, wave functions and electrical conductance in crystals with incommensurate periodic potentials*, *Phys. Rep.* **126**, 189 (1985).
- [18] M. V. Feigel'man, L. B. Ioffe, V. E. Kravtsov, and E. A. Yuzbashyan, *Eigenfunction Fractality and Pseudogap State near the Superconductor-Insulator Transition*, *Phys. Rev. Lett.* **98**, 027001 (2007).

- [19] M. V. Feigel'man, L. B. Ioffe, V. E. Kravtsov, and E. Cuevas, *Fractal superconductivity near the localization threshold*, *Ann. Phys. (NY)* **325**, 1390 (2010).
- [20] M. Tezuka and A. M. A. M. García-García, *Stability of the superfluid state in a disordered one-dimensional ultracold fermionic gas*, *Phys. Rev. A* **82**, 043613 (2010).
- [21] Z. Fan, G.-W. Chern, and S.-Z. Lin, *Enhanced superconductivity in quasiperiodic crystals*, *Phys. Rev. Research* **3**, 023195 (2021).
- [22] X. Zhang and M. S. Foster, *Enhanced amplitude for superconductivity due to spectrum-wide wave function criticality in quasiperiodic and power-law random hopping models*, *Phys. Rev. B* **106**, L180503 (2022).
- [23] S. A. A. Ghorashi, Y. Liao, and M. S. Foster, *Critical Percolation without Fine-Tuning on the Surface of a Topological Superconductor*, *Phys. Rev. Lett.* **121**, 016802 (2018).
- [24] J. F. Karcher and M. S. Foster, *How spectrum-wide quantum criticality protects surface states of topological superconductors from Anderson localization: Quantum Hall plateau transitions (almost) all the way down*, *Ann. Phys.* **435**, 168439 (2021).
- [25] A. Altland, P. W. Brouwer, J. Dieplinger, M. S. Foster, M. Moreno-Gonzalez, and L. Trifunovic, *Fragility of Surface States in Non-Wigner-Dyson Topological Insulators*, *Phys. Rev. X* **14**, 011057 (2024).
- [26] S. Ryu, A. P. Schnyder, A. Furusaki, and A. W. W. Ludwig, *Topological insulators and superconductors: tenfold way and dimensional hierarchy*, *New. J. Phys.* **12**, 065010 (2010).
- [27] D. Bernard and A. LeClair, *A classification of 2D random Dirac fermions*, *J. Phys. A* **35**, 2555 (2002).
- [28] A. P. Schnyder, S. Ryu, A. Furusaki, and A. W. W. Ludwig, *Classification of topological insulators and superconductors in three spatial dimensions*, *Phys. Rev. B* **78**, 195125 (2008).
- [29] A. A. Nersisyan, A.M. Tsvelik, and F.Wenger, *Disorder effects in two-dimensional d-wave superconductors*, *Phys. Rev. Lett.* **72**, 2628 (1994).
- [30] C. Mudry, C. Chamon, and X.-G. Wen, *Two-dimensional conformal field theory for disordered systems at criticality*, *Nucl. Phys.* **B466**, 383 (1996); J. S. Caux, I. I. Kogan, and A. M. Tsvelik, *Logarithmic operators and hidden continuous symmetry in critical disordered models*, *ibid.*, 444 (1996).
- [31] H.-Y. Xie, Y.-Z. Chou, and M. S. Foster, *Surface transport coefficients for three-dimensional topological superconductors*, *Phys. Rev. B* **91**, 024203 (2015).
- [32] X. Zhang, Z. Zhu, J. H. Wilson, and M. S. Foster, *in preparation*.
- [33] V. Mastropietro, *Stability of Weyl semimetals with quasiperiodic disorder*, *Phys. Rev. B* **102**, 045101 (2020).
- [34] Alexander Weiße, Gerhard Wellein, Andreas Alvermann, and Holger Fehske, *The kernel polynomial method*, *Rev. Mod. Phys.* **78**, 275 (2006).
- [35] A. Pieper et al. *High-performance implementation of Chebyshev filter diagonalization for interior eigenvalue computations*, *J. Comput. Phys.* **325**, 226 (2016).
- [36] H. Guan and W. Zhang *Dual applications of Chebyshev polynomials method: Efficiently finding thousands of central eigenvalues for many-spin systems*, *SciPost Phys.* **11**, 103 (2021).
- [37] B. Sbierski, J. F. Karcher, and M. S. Foster, *Spectrum-Wide Quantum Criticality at the Surface of Class AIII Topological Phases: An “Energy Stack” of Integer Quantum Hall Plateau Transitions*, *Phys. Rev. X* **10**, 021025 (2020).
- [38] B. Uchoa, G. G. Cabrera, and A. H. Castro Neto, *Nodal liquid and s-wave superconductivity in transition metal dichalcogenides*, *Phys. Rev. B* **71**, 184509 (2005).
- [39] B. Uchoa and A. H. Castro Neto, *Superconducting States of Pure and Doped Graphene*, *Phys. Rev. Lett.* **98**, 146801 (2007).
- [40] R. Nandkishore, J. Maciejko, D. A. Huse, and S. L. Sondhi, *Superconductivity of disordered Dirac fermions*, *Phys. Rev. B* **87**, 174511 (2013).
- [41] I.-D. Potirniche, J. Maciejko, R. Nandkishore, and S. L. Sondhi, *Superconductivity of disordered Dirac fermions in graphene*, *Phys. Rev. B* **90**, 094516 (2014).
- [42] N. B. Kopnin and E. B. Sonin, *BCS Superconductivity of Dirac Electrons in Graphene Layers*, *Phys. Rev. Lett.* **100**, 246808 (2008); B. Uchoa and A. H. Castro Neto, *Comment on “BCS Superconductivity of Dirac Electrons in Graphene Layers”*, *ibid.* **102**, 109701 (2009); N. B. Kopnin and E. B. Sonin, *Kopnin and Sonin Reply: ibid.* **102**, 109702 (2009).
- [43] M. Tinkham, *Introduction to Superconductivity*, 2nd Ed. (Dover, New York, 2004).
- [44] Valentin Crépel, Aaron Dunbrack, Daniele Guerzi, John Bonini, and Jennifer Cano, *Chiral model of twisted bilayer graphene realized in a monolayer* *Phys. Rev. B* **108**, 075126 (2023).
- [45] T. Devakul and D. A. Huse, *Anderson localization transitions with and without random potentials*, *Phys. Rev. B* **96**, 214201 (2017).
- [46] N. S. Ticea, J. May-Mann, J. Xiao, E. Berg, and T. Devakul, *Stability of quasiperiodic superconductors*, *Phys. Rev. B* **110**, L060501 (2024).
- [47] G. P. Srivastava, *Broyden's method for self-consistent field convergence acceleration*, *J. Phys. A: Math. Gen.* **17** L317 (1984).
- [48] D. D. Johnson, *Modified Broyden's method for accelerating convergence in self-consistent calculations*, *Phys. Rev. B* **38**, 12807 (1988).
- [49] D. J. Scalapino, S. R. White, and S. C. Zhang, *Superfluid Density and the Drude Weight of the Hubbard Model*, *Phys. Rev. Lett.* **68**, 2830 (1992).
- [50] M. S. Foster, Hong-Yi Xie, and Yang-Zhi Chou, *Topological protection, disorder, and interactions: Survival at the surface of three-dimensional topological superconductors*, *Phys. Rev. B* **89**, 155140 (2014).
- [51] Y.-Z. Chou and M. S. Foster, *Chalker scaling, level repulsion, and conformal invariance in critically delocalized quantum matter: Disordered topological superconductors and artificial graphene* *Phys. Rev. B* **89**, 165136 (2014).